POLITECNICO DI MILANO
DEPARTMENT OF INGEGNERIA MECCANICA
DOCTORAL PROGRAMME IN MECHANICAL ENGINEERING

ON THE MODELLING OF DEFORMABLE TYRE ON DEFORMABLE SOIL FOR TREAD PATTERN DESIGN OPTIMIZATION

Doctoral Dissertation of:
Silvia Negrini

Supervisor:
Prof. Francesco Braghin

Tutor:
Prof. Marco Bocciolone

The Chair of the Doctoral Program:
Prof. Bianca Maria Colosimo

2012 – XXV

I would like thank Stefano Melzi and Edoardo Sabbioni, who together with my supervisor prof. Francesco Braghin always supported me during the development of this thesis with their help and guidance.

I would like to thank Maurizio Cutini for his support during the experimental test carried out at the CRA-ING institution.

I would also like to thank Alessandro Tasora for having helped me with the Chrono::Engine library.

I would like to thank prof. Dan Negrut and all the guys from the lab, in particular Hammaz Mazhar for his support with the GPU programming and Arman Pazouki and Rebecca Shotwell for beeing my guides in discovering Madison life.

Finally I would like to thank all my friends and my collegues, especially guys from the Tropical Office, for making my PhD a lot more fun.

Abstract

AGRICULTURAL tyres should satisfy many different requirements, such as to provide good traction performance, to limit soil sinkage and compaction, and to guarantee good comfort level, avoiding high vibrations transmission to the driver seat. The achievement of all these requirements is strongly dependent on tread design, and of course also on soil properties.

At present, no numerical approach is available to predict traction properties as a function of tread design, thus requiring the production of several test prototypes. A first attempt to numerically predict tyre-soil contact forces has been done by schematizing the ground as a deformable springs layer and the tyre as a deformable ring reproducing the tread geometry. Moreover, only the purely longitudinal behavior has been investigated. Thus, an in-plane tire model has been considered, to study traction properties, comfort, and soil compaction.

Then, a tridimensional model has been studied, modeling the soil as a particles cluster, interacting with each other. To state this model a C++ multi-body library, based on differential variational inequalities, has been accounted. The simulation of a direct shear test has been carried out with this model, to study the influence of numerical parameters on soil modeling, and to show the potentials of this model to study subsoil behaviour.

Summary

TYRES of off-road vehicles, in particular of agricultural tractors, should satisfy many different requirements; moreover their performance is significantly affected by soil conditions, which can highly vary as a function of humidity and temperature [34].

First, the tyres passage should not overly degrade soil conditions, indeed soil strain and compaction due to tyres passage affect soil by decreasing water infiltration and water holding capacity, increasing runoff and erosion, leading to a rise in crop production problems, thereby decreasing crop yields and profitability of farming systems.

Moreover, when plastic flow occurs, although soil is not compacted, the strain may decrease the connectivity of pores in the soil, thereby decreasing the water infiltration rate [55].

Also, the tyres should provide a limited level of vibrations, since the vibrations trasmitted by the tyre impact on ride comfort, and the exposure to significant levels of acceleration for a long time affects the efficiency and the alertness of the operators [41] leading also to unsafe situations.

Finally the tyres should guarantee good traction performance, indeed variations of the normal contact forces due to vertical tyre displacements result in variations of the traction force provided by the tyres which influences the quality of tillage and other operations.

Hance the aim of this thesis is to state a model able to predict the impact of tyre structure and tyre tread pattern, depending on soil characteristics, on:

- vibrations transmission,
- tractive performance,
- soil compaction and sinkage.

To this purpose in this thesis two tyre-soil interaction models will be proposed.

The first model that will be discussed is a plane model, considering the forces and displacement in vertical and longitudinal directions.

This model can be outlined as composed by two sub-models interacting with one another: the first one models the tyre structure and tread pattern geometry whereas the second one represents the soil.

The tyre model allows to take into account the effect of the tread pattern design, so that the excitation of the vertical dynamics associated with lugs geometry can be included. Moreover the tyre model considers the tyre structure through the eigenfrequencies and eigenvalues resulting from the analysis of an impulsive response of a real agricultural tyre.

The soil model represents the soil as a plane surface, whose nodes can be displaced vertically under the tyres load, reacting with shear and normal stresses.

The shear and normal responses of the soil have been characterized by two tests: respectively the direct shear test, performed to measure the shear resistance of a soil under pressure, and the cone penetrometer test, allowing to measure the normal resistance of the soil to the sinkage of a conic pin.

Through those tests it has been possible to set the parameters of the numerical model of the tyre-soil interaction, based on Matlab language.

Finally, a particles model has been stated to simulate the soil dynamics. This model is based on a multi-body C++ library, Chrono::Engine, representing bodies interaction by means of differential variational inequalities theory.

The main advantages presented by this model are the possibility of considering the soil displacement and stress distribution in subsoil layers and the capability to introduce in the formulation the tridimensionality of the problem, allowing to consider the lateral forces involved in more complex maneuvers than forward ride, alhtough at the moment the focus is pointed on the soil dynamics.

The rest of this thesis will be structured as hereby follows:

- in chapter 1 the state of the art of previous models for the tyre-soil interaction will be presented;

- in chapter 2 the experimental tests carried out on soil and tyre will be discussed, in order to introduce the results in the plane model of the tyre-soil interaction;
- in chapter 3 the plane model for tyre-soil interaction will be stated, thus simulation results provided by this model will be shown;
- in chapter 4 the particles model staded on the basis of the DVI formulation will be presented.

Contents

1 State of the art **1**
1.1 Tyre-soil interaction models 2
  1.1.1 Rigid wheel at rest 3
  1.1.2 Rigid wheel at driving state 4
  1.1.3 Rigid wheel at braking state 7
  1.1.4 Deformable tyre 9
1.2 Experimental tests 11
1.3 Tread pattern optimization 13

2 Experimental tests **17**
2.1 Soil tests 18
  2.1.1 Cone penetration test 18
  2.1.2 Direct shear test 20
2.2 Tyre test 22
  2.2.1 Impulsive test 22
  2.2.2 Least square exponential method 24
2.3 Traction test 27

3 Planar model **31**
3.1 Tyre model 32
  3.1.1 Tread pattern 32
  3.1.2 Tyre structure 37
3.2 Soil model 39
  3.2.1 Normal stress 40

3.2.2 Shear stress 41
3.3 Tyre-soil interaction 43
3.4 Model validation 45
3.5 Pattern sensitivity analysis 47
3.5.1 Traction force 48
3.5.2 Standard deviation of the hub acceleration 51
3.5.3 Sinkage 54
3.5.4 Sensitivity analysis conclusions 57
3.6 Whole tractor model 57
3.6.1 Tractor multi-body model 58
3.6.2 Tractor multi-body model validation 59
3.6.3 Tractor multi-body model simulation 61
3.7 Conclusions 64

4 Particle Model **65**
4.1 Differential Variational Inequalities 66
4.1.1 Problem formulation 66
4.1.2 Constraints formulation 67
4.1.3 The overall model 69
4.1.4 Time-stepping scheme 70
4.2 Simulations 71
4.2.1 Simulation data 71
4.2.2 Simulation results 73
4.2.3 Conclusions 80

5 Conclusions **83**

Bibliography **93**

CHAPTER 1

State of the art

Agricultural tractors should satisfy many different requirements, achieving a good tractive pull, guaranteeing a safe comfort level for the operator and avoiding a large soil compaction, which leads to difficulties for plants roots growth [11] [46].

Moreover, those achievements should be satisfied working over different soils whose properties can significantly vary depending on terrain composition, air humidity, and temperature conditions. Furthermore, in the last twenty years the tractors speed has increased, involving an increase in comfort problems related to dynamic tractor behavior and drivers vibration exposure [50], which affects the operator health, potentially causing several damages to low back, neck, shoulders and thoracic regions [38] [43].

The tractor tyres play a decisive role to face those achievements, indeed tyres size and structure influence the terrain cone index (CI) value and the topsoil compaction [46] [5], while the tyres stiffness and treads pattern influence the tractor dynamics behavior [21].

An accurate tyre-soil interaction model can lead to understanding how tyre types and terrain conditions affect the mobility, the tractive performances, and the soil compaction [57], although the large variance in soils behavior impose several difficulties for predictive studies [35].

Hence in the last sixty years many research works studied the tyre-soil contact issue, considering both the numerical and the experimental approaches.

1.1 Tyre-soil interaction models

Studies of the interaction between the tyre and the deformable soil have been developed since the sixties.

The first proposed models were mainly based on Bekker and Coulomb equations to calculate respectively the normal pressure and the shear stress in the soil beneath the tyres. The Bekker equation [10] allows to compute the normal pressure σ as a function of the soil sinkage z, as shown in equation 1.1, where the parameters k_c, k_ϕ, and n are associated to the soil properties and can be determined by a dynamice plate loading test, while B is the tyre width.

$$\sigma = \left(\frac{k_c}{B} + k_\phi\right) z^n \tag{1.1}$$

The shear stress may be instead computed through the Coulomb equation, modified according to the Janosi and Hanamoto work [32] to take into account the influence of the shear displacement j, as shown in equation 1.2, where $k_{cohesion}$ and ϕ are respectively the cohesion and the free angle of shearing resistance of the soil, and K is the soil shear deformation paramenter [32].

$$\tau = \left[k_{cohesion} + \sin\left(\phi\right)\sigma\right] \cdot \left(1 - e^{j/K}\right) \tag{1.2}$$

These equations allowed to compute the stress at the interface between the tyre and the soil as a function of the soil sinkage caused by the tyre, thus it is necessary either to state some hypothesis on the shape of the contact interface or consider the equilibrium of each point of the tyre surface.

The simpliest model considers a slick rigid tyre, taking into account three different conditions:

- at rest,
- at driving state,
- at braking state.

In the next subsections (1.1.1, 1.1.2, 1.1.3), will be presented the calculation for the stresses σ and τ in the three just listed conditions, according to the work of Muro and O'Brien [40].

1.1.1 Rigid wheel at rest

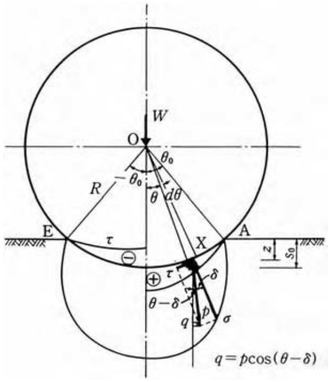

Figure 1.1: *stress distribution beneath a tyre at rest [40]*

In the case of a rigid tyre at rest under an axle load W, the soil develops a reaction force, which is the product of a symmetrical distribution of the normal stress σ and of the shear resistance τ, shown in figure 1.1. The sign of the shear resistance τ should be reversed for the left and right side of the wheel, such that the torque resulting from the integration of the shear resistance becomes zero.

The resultant stress p, due to the normal stress σ and to the shear stress τ, at an arbitrary point X of the contact surfarce, is inclined of an angle δ, as shown in equation 1.3.

$$\delta = \arctan\left(\frac{\tau}{\sigma}\right) \tag{1.3}$$

To account for the modulus of the stress at an arbitrary point X it is required to know the amount of sinkage and the slippage at that point.

The amount of sinkage z can be calculated as in equation 1.4, where θ_0 is an half of the angle subtending the contact surface, θ is the central angle of the point X, and R is the wheel radius; while the amount of slippage can be calculated as a function of the center angle, as in equation 1.5.

$$z = R\left[\cos\left(\theta\right) - \cos\left(\theta_0\right)\right] \tag{1.4}$$

$$j_0 = R\left[\theta_0 - \sin\left(\theta\right)\right]\frac{\theta_0 - \theta}{\theta_0} \tag{1.5}$$

The vertical component $q\left(\theta\right)$ of the resulting stress, can be computed from the Bekker equation (see eq. 1.1), thus the resulting stress $p\left(\theta\right)$ can be calculated as in 1.6.

$$p(\theta) = \frac{q(\theta)}{cos(\theta - \delta)} = \left(\frac{k_c}{B} + k_\phi\right) \frac{z^n}{cos(\theta - \delta)} \tag{1.6}$$

The distribution of stresses σ and τ can be iteratively calculated until the load on the axle W is equilibrated by the vertical reaction of the soil F_z, resulting from the integration of the vertical component of the stress $p(\theta)$ along the contact surface between $-\theta_0$ and $+\theta_0$, as in equation 1.7, where B is the wheel width.

$$F_z = BR \int_{-\theta_0}^{+\theta_0} p(\theta) \cos(\theta - \delta) \cos(\theta)\, d\theta \tag{1.7}$$

1.1.2 Rigid wheel at driving state

In the case of a wheel at driving state, the procedure is similar to the one applied for a wheel at rest, although the non-symmetry of stress distribution must be accounted.

The amount of slippage j_d at an arbitrary point X of the contact surface results from the integration of the slip velocity v_s, that can be expressed as in equation 1.8, where ω is the angular velocity of the wheel, v is the forward speed, and θ is the central angle of the point X, as in figure 1.2.

$$v_s = R\omega - v\cos(\theta) \tag{1.8}$$

As $R\omega > v$ for the driving state, it is possible to define the slip ratio i_d as shown in equation 1.9, thus by substituting it in eq. 1.8, v_s can be expressed as in equation 1.10.

$$i_s = 1 - \frac{v}{R\omega} \tag{1.9}$$

$$v_s = R\omega\left[1 - (1 - i_d)\cos(\theta)\right] \tag{1.10}$$

By integration of the slip velocity v_s it is possible to calculate the amount of slippage (see eq. 1.11), whose distribution is represented in figure 1.2. Thus it is possible to calculate the shear stress distibution from the Mohr-Coloumb equation modified according to Janosi (eq. 1.2).

Equation 1.11 shows the integration of the slip velocity v_s from the beginning of the contact to the instant t, which can be solved as a function of the central angle, from the instantaneous angle θ to the entering angle θ_f, as shown in figure 1.2.

$$\begin{aligned} j_d &= R\int_0^t \omega\left[1-(1-i_d)\cos(\theta)\right]dt = \\ &= R\int_\theta^{\theta_f} \omega\left[1-(1-i_d)\cos(\theta)\right]d\theta = \\ &= R\left\{\theta_f-\theta-(1-i_d)\left(\sin(\theta_f)-\sin(\theta)\right]\right\} \end{aligned} \tag{1.11}$$

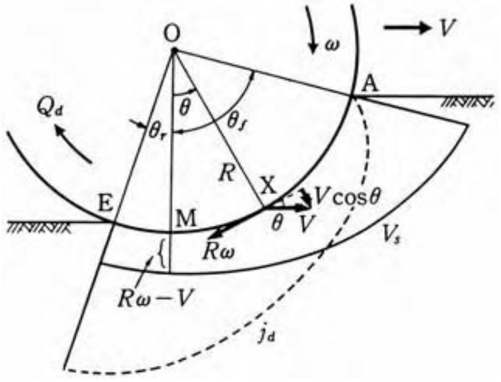

Figure 1.2: *the distribution of the amount of slippage under a rigid wheel at driving state [40]*

The sinkage, required to account for the vertical component of the resulting stress $p(\theta)$, can be calculated as the length of the vertical component $d(\theta)$ of the trajectory of a point on the peripherical surface of the wheel during the contact with the soil.

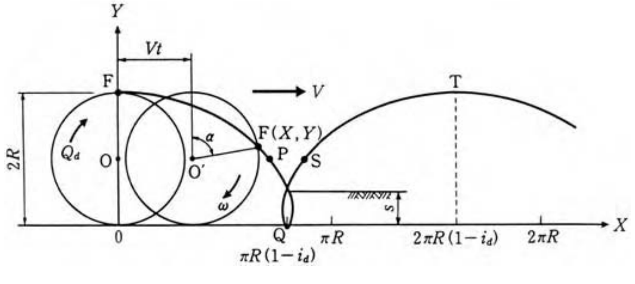

Figure 1.3: *the trajectory of a point F on the peripherical surface of the wheel at driving state [40]*

Figure 1.3 shows the rolling locus of a point on the peripherical surface of the wheel, whose length can be calculated as in equation 1.12, where the trajectory is integrated from the beginning of the contact at point a to the point b.

$$l\left(\theta\right) = \int_{a}^{b} \sqrt{1 + \left(\frac{dY}{dX}\right)^2} dX \tag{1.12}$$

The coordinates of a point on the peripherical surface of the wheel are the coordinates of a point on a trochoid curve. Their values can be expressed as in equations 1.13 and 1.14, thus it is possible to express the derivative $\frac{dY}{dX}$ as in equation 1.15.

$$X = \frac{v\alpha}{\omega} + R\sin\left(\alpha\right) = R\left[\alpha\left(1 - i_d\right) + \sin\left(\alpha\right)\right] \tag{1.13}$$

$$Y = R\left[1 + \cos\left(\alpha\right)\right] \tag{1.14}$$

$$\frac{dY}{dX} = -\frac{\sin\left(\alpha\right)}{1 - i_d + \cos\left(\alpha\right)} \tag{1.15}$$

Hence the traveled length of the trajectory can be accounted as in equation 1.16, after changing the integration domain from the abscissa of the trajectory X to the rotation angle of the wheel α

$$l\left(\theta\right) = \int_{\alpha_f}^{\alpha} \sqrt{1 + \left[-\frac{\sin\left(\alpha\right)}{1 - i_d + \cos\left(\alpha\right)}\right]^2} \cdot R\left[1 - i_d + \cos\left(\alpha\right)\right] d\alpha \tag{1.16}$$

The vertical component $q\left(\theta\right)$ of the stress can be calculated as in equations 1.17 and 1.18, valable respectively before and after the maximum sinkage point.

$$\text{For} \quad \theta_{max} \leq \theta \leq \theta_f \qquad q\left(\theta\right) = k_1\xi\left[d\left(\theta\right)\right]^{n_1} \tag{1.17}$$

$$\text{For} \quad -\theta_r \leq \theta \leq \theta_{max} \qquad q\left(\theta\right) = k_1\xi\left[d\left(\theta\right)\right]^{n_1} + + k_2\xi\left[d\left(\theta_{max}\right) - d\left(\theta\right)\right]^{n_2} \tag{1.18}$$

The coefficients k_1 and k_2 correspond to the behaviour of the soil respectively before and after reaching the maximum sinkage, and can be calculated from equations 1.19 and 1.20, where $k_{c,1}$, $k_{\phi,1}$, $k_{c,2}$, and $k_{\phi,2}$ are the Bekker equation coefficients and can be inferred from a dynamic plate loading test, as well as the coefficient ξ in the equation 1.17 and 1.18.

$$k_1 = \left(\frac{k_{c,1}}{B} + k_{\phi,1}\right) \tag{1.19}$$

$$k_2 = \left(\frac{k_{c,2}}{B} + k_{\phi,2}\right) \tag{1.20}$$

The resulting stress $p(\theta)$ can now be calculated from the equation 1.21, where δ, θ, and ζ, are respectively the angle between the shear stress and the normal stress, the center angle, and the angle between the longitudinal force and the normal load W (see eq. 1.22)

$$p(\theta) = \frac{q(\theta)}{\cos(\zeta + \theta - \delta)} \tag{1.21}$$

$$\zeta = \arctan\left(\frac{T_d}{W}\right) \tag{1.22}$$

1.1.3 Rigid wheel at braking state

The distribution of the amount of slippage beneath a rigid wheel at braking state is asymmetrical, as well as under a rigid well at driving state; moreover the slip velocity presents a change of sign, as shown in figure 1.5.

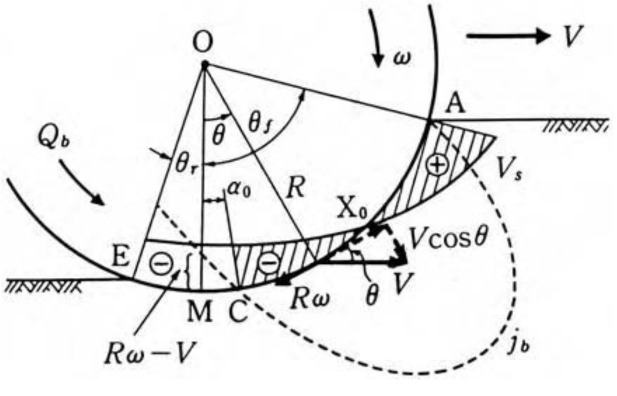

Figure 1.4: *the distribution of the amount of slippage under a rigid wheel at braking state [40]*

Since $R\omega < V$, the slip ratio i_b can be accounted as in equation 1.23, thus the slip velocity v_s, defined in equation 1.8, can be expressed as in 1.24.

$$i_b = \frac{R\omega}{v} - 1 \tag{1.23}$$

$$v_s = R\omega\left[1 - \frac{1}{1 + i_b}\cos(\theta)\right] \tag{1.24}$$

By zeroing the slip velocity, it is possible to point out the value θ_0 of the center angle corresponding to the point on the contact surface where the velocity sign change is located (see eq. 1.25).

$$\theta = \arccos\left(\frac{R\omega}{v}\right) = \arccos\left(1 - i_b\right) \tag{1.25}$$

The amount of slippage results from the slip velocity integration from the center angle θ to the entering angle θ_f, as in equation 1.26.

$$\begin{aligned} j_b &= R\int_0^t \omega\left[1 - \frac{1}{1+i_b}\cos\left(\theta\right)\right]dt = \\ &= R\int_\theta^{\theta_f} \omega\left[1 - \frac{1}{1+i_b\cos\left(\theta\right)}\right]d\theta = \\ &= R\left\{\left(\theta_f - \theta\right) - \frac{1}{1+i_b}\left[\sin\left(\theta_f\right) - \sin\left(\theta\right)\right]\right\} \end{aligned} \tag{1.26}$$

The length of the trajectory projected in vertical direction is accounted for the sinkage calculation. The trajectory of a peripherical point of the wheel is a trochoidal curve, as well as in subsection 1.1.2, although slight differences due to the different slip ration i_b, as it can be observed in figure 1.5.

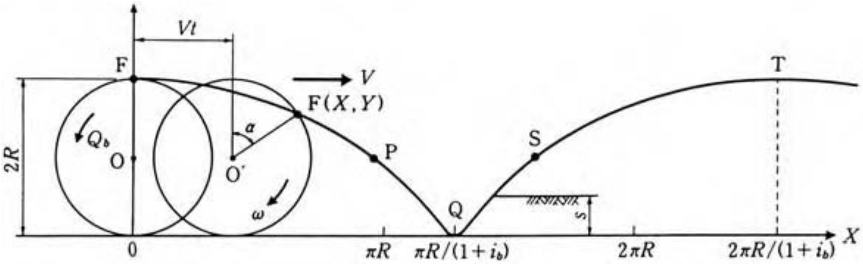

Figure 1.5: *the trajectory of a point F on the peripherical surface of the wheel at braking state [40]*

The coordinates of the trochoidal trajectory are shown in equations 1.27 and 1.28, as well as their derivative $\frac{dY}{dX}$ in equation 1.29, which is used to determinate the length of the traveled trajectory $l\left(\theta\right)$ in equation 1.30.

$$X = \frac{v\alpha}{\omega} + R\sin\left(\alpha\right) = R\left[\alpha\left(1+i_b\right) + \sin\left(\alpha\right)\right] \tag{1.27}$$

$$Y = R\left[1 + \cos\left(\alpha\right)\right] \tag{1.28}$$

$$\frac{dY}{dX} = -\frac{\sin(\alpha)}{\frac{1}{1+i_b} + \cos(\alpha)} \tag{1.29}$$

$$l(\theta) = \int_{\theta}^{\theta_f} \sqrt{\left[\frac{1}{1+i_b}\right]^2 - \frac{2\cos(\theta)}{1+i_b} + 1} \quad d\theta \tag{1.30}$$

The vertical component of the stress $q(\theta)$ can be calculated from the projection of $l(\theta)$ in vertical direction as explained in equations 1.17 and 1.18 for a wheel at driving condition. Thus the resulting stress $q(\theta)$ can be accounted as shown in equations 1.31, 1.32 and 1.33.

$$p(\theta) = \frac{q(\theta)}{\cos(\varsigma - \theta + \delta)} \tag{1.31}$$

$$\varsigma = \delta + \eta - \pi/2 \tag{1.32}$$

$$\begin{aligned} \eta &= \arctan\left(\frac{v\sin(\theta)}{R\omega - v\cos(\theta)}\right) = \\ &= \arctan\left(\frac{\sin(\theta)}{1 + i_b - \cos(\theta)}\right) \end{aligned} \tag{1.33}$$

1.1.4 Deformable tyre

The model presented in the previous section (sec. 1.1) works with a fixed geometry of the contact surface, thus it applies also to the case of deformable tyre, provided to state some hypothesis about shape of the interaction surface.

Schmid in a review paper [49] presented three possible simplified shapes of the tyre, shown in figure 1.6.

- Model a of figure 1.6 proposes to model the contact surface as a plane.
- Model b, considers the contact surface as the peripherical surface of a rigid wheel, whose radius is larger than the one of the tyre under examination.
- Finally model c depicts the contact surface as a parabolic curve.

These models are simple and perform good results, however they apply only to the case of slick wheel, since the presence of the lugs is not accounted for the integration of the slip velocity.

To overcome this limit, El-gawwad et al. [25] [26] [27] proposed a multi-spoke model able to predict the steady state performance of the tyre, considering also the lugs inclination.

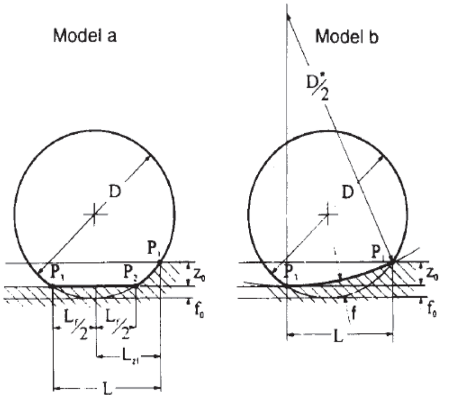

Figure 1.6: *three different models of the contact surface shape between tyre and soil [49]*

As remarked by Schmid [49], these analytical models presume an a priori knowledge of the contact contour geometry, and do not address the fact that the geometry of the contact area results from deformation of the tyre and deformation of the soil due to the interactio of both.

To solve this issues a different approach is required to model the soil and the tyre; the first one considered is the finite elements method.

In the nineties Aubel [7] [8] [9] developed a finite elements model, called VENUS (VEhicle NatUre Simulation), able to calculate the soil and tyre deformations in vertical and horizontal directions, taking into account also the bulldozing effect.

Mohsenimanesh et al. [39] in 2009 developed a finite element model able to predict the pressure on the soil surface, which have a strong influence on soil compaction, also considering many soil layers with different properties.

Xia [57] in 2010 modelled both the tyre and the soil by finite elements, considering a mesh more refined for the topsoil than for the undersoil, to decrease the computational cost of the model.

To reduce the simulation computational effort, the soil can also be modeled as a plane mesh, whose nodes are able to move in vertical direction; this kind of model, called digital elevation model, was proposed by Jain and al. [31, 53] for the wheel-soil interaction in the case of planetary rovers and implemented in the ROAMS planetary rover simulation environment.

Recently also the discrete elements method has been proposed to model the soil [33]. This technique differs from finite elements because it considers many discontinuos bodies interacting with one another and was firstly porposed by Cundall et al. [22] in 1971.

The main critical issue of finite and discrete elements models is the ground discretisation [49], because a high number of elements is required to perform a good approximation of the soil behaviour, involving high computational effort.

1.2 Experimental tests

Beside the numerical and analytical models, during the last 60 years many different experimental tests have been carried out in order to study the tyre-soil interaction, in particular focusing on the stress and strain distribution beneath the tyre, having a strong impact on soil compaction, traction, and vibrations transmission.

Botta et al. [12] [13] studied the influence of soil state on tyre-soil interaction, testing three different soil conditions:

- direct sowing condition,
- seedbed condition,
- ploughed soil.

The comparison among these soil conditions prooved that residual topsoil bulk density and tire sinkage affect largely loose soils, leading to a greater rise of soil compaction and motion resistance.

Many experimental tests focused on the residual compression of the soil, measured by the bulk density and the cone index, after tyre passage, since it has a very defavorable effect in the roots growth.

The subsoil and the topsoil compactions are related to different factors: the topsoil compaction increases when the ground pressure rises, whereas the subsoil compaction is more affected by the dynamics load on the tyre, as shown by Way et al. [56]. Although this result was partially disproved by Arvidsson and Keller [3], who stated that neither topsoil stress is simply a function of inflation pressure, nor subsoil stress is simply a function of wheel load.

The ground pressure is quite affected by the inflation pressure [4]: hence decreasing the inflation pressure reduces the effect on soil physical properties, although a low inflation pressure decreases the tyre life expectancy [20].

Moreover, it has been possible to state that the subsoil compaction does not depend on vehicle ground pressure, which instead influences the topsoil compaction, and to prove that the magnitude of change in bulk density and cone index values are reduced by lowering inflation pressure and increasing tyre size.

Smerda and Cupera agreeded with this conclusion in their study of the influence of tyre inflation pressure on drawpull bar [52], proving that the enlargement of the contact area between the tyre and the soil reduces the rolling resistance on loose soil and restricts physical degradation of soil characteristics.

Among the consequeces of tyre passage on loose soil, also the soil displacement plays an important role.

Way et al. [55] observed that the initial and final soil bulk density information alone may not reflect the strain beneath the tyre, indeed the loose soil is compressed in the vertical and longitudinal directions and elongated in the lateral direction.

The distribution shape of normal and shear stresses around the circumference of soil-tyre contact patch depends on tyre configurations (size, load stiffness, and slip), soil conditions, and operational driving conditions of vehicles. For tyre with high inflation pressure the maximum soil stress occurs in front contact region near the center line of wheels, whereas the stress distribution under tyre with low inflation pressure appears to be uniform in the main region of contact surface.

On soft clay soil both normal and shear stresses increase very fast and decrease immediately after reaching the maximum value implying that the plastic flow occured under tractor tyres, whereas on hard clay soil the form of soil stress distribution is more uniform, as in the case in firm sandy loam [42].

Another interesting aspect of this problem is the vibrations transmission from the soil to the driver, since the discomfort can have severe consequences on driver health.

Nguyen and Inaba [41] carried out a series of experiments with different inflation pressure on road and on sandy loam, proving that the main excitations are due to lugs and tyre eccentricity, if present.

The main frequency exciting the system are shown in equations 1.34 1.35 and 1.36: the first one is the frequency of wheel-tyre assembly and depends on the angular velocity of the tyre ω, whereas the second and the third ones are respectively the first and second order excitation frequencies of tyre lugs, whose number is n.

$$f_w = \frac{\omega}{2\pi} \tag{1.34}$$

$$f_{L1} = \frac{n\omega}{2\pi} \tag{1.35}$$

$$f_{L2} = \frac{n\omega}{\pi} \tag{1.36}$$

Nguyen ad Inaba evaluated the influence of lugs and tyre eccentricity on the root mean square values of the acceleration, considering separately different dynamics behaviours:

- the root mean square of the dynamic wheel load is proportional to forward speed in the case of high tyre inflation pressure.
- the root mean square of the bounce acceleration is proportional to forward speed and inversely proportional to tyre inflation pressure.
- the root mean square of the roll and pitch accelerations is proportional to forward speed in the case of low inflation pressure, other wise the root mean square of accelerations is not strictly proportional to forward speed.

The eventual non-uniformity of the tyre strongly affects the wheel-load variations at the first order frequency and harmonics, furthermore this effect increases as the tyre inflation pressure decreases or the forward speed increases; besides this effect becomes critical as the tractor moves on soft sandy loam.

The experimental tests presented in this section allowed to enlarge the knowledge and comprehension of this complex phenomenon, providing usefull tools to state more accurate models.

1.3 Tread pattern optimization

Soil-tyre contact area and pressure are important factors in the compaction induced by the traffic of agricoltural machinery and both depend in tyre type and size, static load, inflation pressure, and soil condition, as shown by Rodriguez et al. [47].

In their study Rodriguez and his collegues reviewed the main mathematical models used to determine the size of the soil-tyre contact surface (A_T).

The first model has been proposed by Mckyes [37], and was based on the section width (B) and on the diameter (d_E) of the tyre, as shown is equation 1.37, where the factor k is a constant equal to 4 for movement on a rigid surface and 2 for movement on loose soil.

$$A_T = \frac{Bd_E}{k} \tag{1.37}$$

The second model has been proposed by Palancar [44] and considers the main dimensions of the footprint, as in equation 1.38, where B and l are respectively the width and length of the footprint, and k is the same constant than in equation 1.37.

$$A_T = kBl \tag{1.38}$$

These equations were developed by interpoolating experimental results for traction tyre; hence these models are inadequate to determine the size of the contact surface of different kind of tyres, such as trailer tyres [23], because traction and transport tyres differ in size structure, working pressure, stiffness and loading capacity.

Rodriguez et al. [47] tested four different tread patterns, shown in figure 1.7, to state regression equations relating contact area, contact pressure and footprint dimension with tyre type, inflation pressure p_i, static load W and section width B.

The four tyres tested in the research are trailer tyres used in for sugarcane harvest and transportation, and have been classified as:

- tyre A: 560/80D26 tyre with block-shape tread pattern.
- tyre B: 23.1-26 tyre with rib shape tread pattern.
- tyre C: 600/50-22.5 tyre with low lug.
- tyre D: 23.1-26 tyre with high lug.

Rodriguez and his collegues prooved that among the four tyre types tested, the block-shape tread pattern and rib-shape tread pattern tyres (A and B tyres) are the best options for sugarcane transport trailers because they cause lower contact pressure, transmit less stress to the soil and hence cause less soil compaction.

The influence of tread pattern on tyre performance was studied also by El-Gawwad et al., who presented a multi-spoke tyre model and studied the influence of angled lugs on performances, focusing on traction tyres [27].

The El-Gawwad work showed that angled lugs are less effective in providing high tractive force than straight lugs, but allow larger lateral forces, which are necessary to keep the tractor on its contour line on a slope.

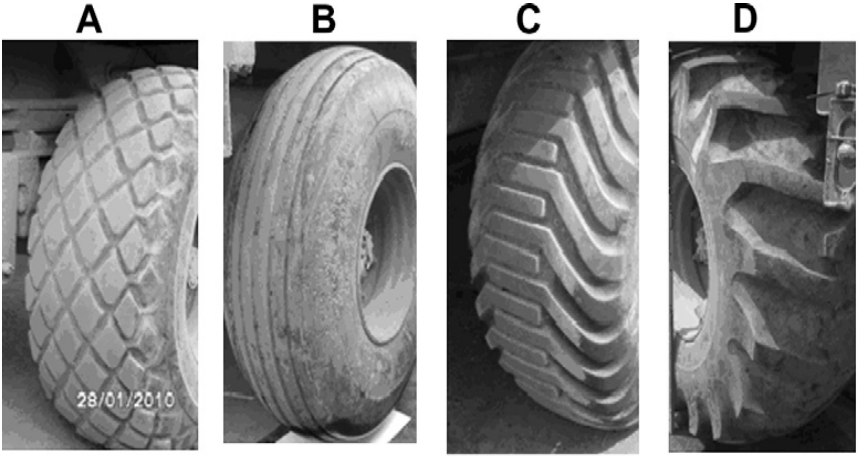

Figure 1.7: *the four tread pattern tested by Rodriguez and alt [47]*

This research has been considered for the tread pattern optimization in this thesis. Since the interest will be focused on traction tyre, the shape of tyre C in figure 1.7 will be considered, and the effect of the lugs length and inclination will be studied.

CHAPTER 2

Experimental tests

Experimental tests are currently used to gather information on the tyre and soil behaviour, as shown in section 1.2.

To state the numerical models that will be presented in chapters 3 and 4, four different tests have been carried out.

1. Cone penetrometer test.
2. Shear test.
3. Impulsive test.
4. Traction test.

The cone penetrometer and shear tests are designed to define the soil properties, the impulsive test allows to characterize the structural properties of a tyre, whereas the traction test measures the traction force exerted by a tractor as a function of tyre and soil properties for different values of the slippages.

The results of those tests allowed to validate the planar model of tyre-soil interaction that will be discussed in chapter 3.

The traction test was simulated with this model, whose parameters were set according to the results of the tests carried out on the tyre mounted on the tractor and on the soil where the traction test was performed.

The next sections (section 2.1 and section 2.2) will be spent to explain these experiments, pointing out the results obtained.

2.1 Soil tests

The main features involved by the soil model are the calculation of the normal stress and the determination of the shear resistance, hence to set the model parameters two tests have been carried out.

The cone penetration test allows to find out the soil resistence to the penetration of a conic tip, thus it is possible to use the results of this test to set the stiffness of the soil, whereas the direct shear test is a useful tool to state the relationship between shear displacement and shear stress.

2.1.1 Cone penetration test

The cone penetrometer test is designed to infer the penetration resistance of the soil [40].

Figure 2.1 depicts a portable cone penetrometer apparatus, whose end is a cone of base area A and apex angle α: the standard dimensions of the end are 6.45cm^2 of area and 30°of apex angle.

At the upper end of the penetrometer a proving ring is mounted: a gauge measures the deformation of a spring, to account for the resistence P provided by the soil to the tip forced in the ground at a constant speed of 1.0cm/s.

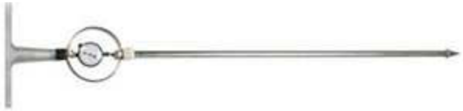

Figure 2.1: *Conic penetrometer.*

From this test the penetration pressure acting under the base of the cone is inferred from the ratio between the penetration force P and the area of the cone base A, usually called cone index CI (equation 2.1).

$$CI = \frac{P}{A} \tag{2.1}$$

Moreover the cone penetrometer test can evaluate the runability of a soil, for instance table 2.1 shows the cone index required to allow the trafficability of different vehicles.

Table 2.1: *cone index required for construction machine trafficability [40]*

Construction machine and situation	Cone Index CI [kN/m^2]
Bulldozer running on very weak terrain	$\geq$196
Bulldozer running on weak terrain	$\geq$294
Middle size bulldozer	$\geq$490
Large size bulldozer	$\geq$686
Scrape dozer running on weak terrain	$\geq$392
Scrape dozer	$\geq$588
Towed scraper	$\geq$686
Motor scraper	$\geq$906
Dump truck	$\geq$1170

To set the soil parameters in the planar model, the penetrometer test was carried out on the soil where the traction test was performed. The results of that test are shown in figure 2.2, where the trend of the soil pressure is draft as a function of the sinkage.

It is possible to infer the presence of three different soil layers:

- the first layer is between 0 and 15cm of sinkage and presents a stiffness of 13.0MPa/m.
- the second layer is between 15 and 24cm and is softer than the first one; the slope in this layer is negative and its mean value is -9.2MPa/m.
- in the third layer the soil stiffens and presents a stiffness of 19.5MPa/m.

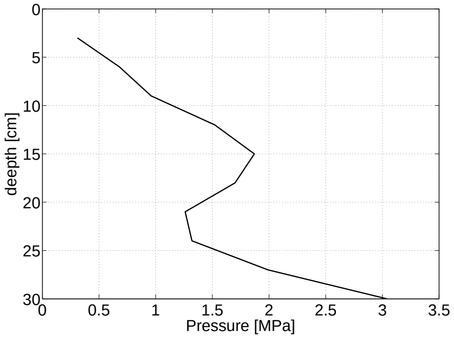

Figure 2.2: *test results: resistence of the soil as a function of the penetrometer sinkage.*

The tractor tyres sinkage usually is limited to 12-15cm, hence to set the model the stiffness of the first soil layer will be considered.

2.1.2 Direct shear test

The direct shear test is designed to study the relationship between shear stress and shear displacement [40].

The test apparatus is depicted in figure 2.3: it consists of two disconnected boxes, which can be filled with a soil sample at a certain density. If a static normal load P is applied to the specimen through a platen and the lower box is moved laterally, a shearing action in the horizontal plane rises. Thus the relationship between the shear force T and the horizontal displacement of the lower box can be inferred [40].

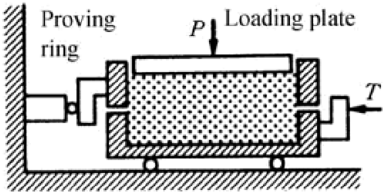

Figure 2.3: *direct shear box apparatus [40].*

Generally the force P is exerted through a gravity operated level, and the force T is tipically measured by use of a proving ring. The horizontal displacement of the lower box and the vertical displacement of the loading plate, necessary for the measurement of the volume change of the soil, can be carried out by the use of two dial gauges.

The experiment is tipically performed with a shearing speed between of maximum 0.2mm/min, as prescripted by the ASTM standard [6].

Figure 2.4 shows the general pattern of results achieved using this apparatus. In the diagram the relationship between shear resistance $\tau = T/A$ (where A is the shearing area) and horizontal displacement, at constant normal stress ($\sigma = P/A$), is shown.

Typically two different responses are obtained. Referring to figure 2.4 in type A soils, the shear resistance τ tends towards an asymptote. This behaviour is typical of normally consolidated clays and loosely accumulated sandy soils.

On the contrary, the shear resistance τ of type B soils typically shows a marked peak at certain horizontal displacement. These hump type behaviours can be usually observed in overconsolidated clays and compacted sandy soils.

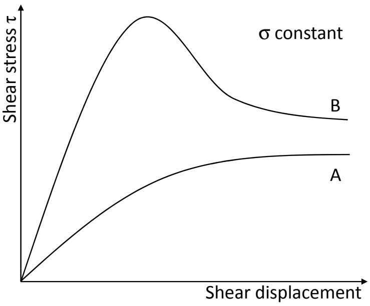

Figure 2.4: *relationship between shear stress and shear displacement.*

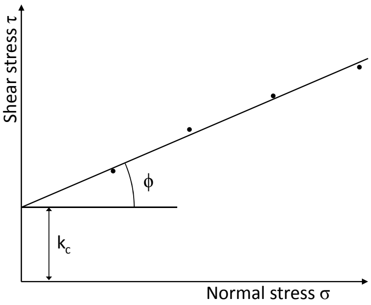

Figure 2.5: *relationship between shear stress and normal stress.*

From these curves, the cohesion k_c and the angle of internal friction ϕ can be identified through the use of Coulomb's failure criterion (see equation 3.26).

The shear test is repeated for a number of normal force values P, to record the peak shear resistance and then to plot the resulting data on a graph.

Figure 2.5 plots the peak shear resistance τ_{max} for B type soil against the normal stress σ. The shear resistance value τ is the one measured at horizontal displacement of 8 mm (or 50% of the initial thickness of the soil sample) for A type soil.

This test was carried out on a sample of the soil where the traction test used for the planar model validation was performed. The soil can be defined as gravel and pebbles in a matrix of silty sand and loose clay, thus is shows the behaviour of type A soils.

After removing the pebbles of dimension larger than 2.00 mm, three prismatic specimens were prepared of quadratic base: 60.00 mm of large and 25.00 mm of height.

The shear speed selected was 4.00 μ/min and the test ended when a shear displacement of 4.00 mm was reached.

Figure 2.6 shows the results of the direct shear test, carried out for three different values of the normal pressure, so that the relationship between the shear stress and the shear displacement can be carried out as a function of the normal pressure. This results will be included in the model in chapter 3.

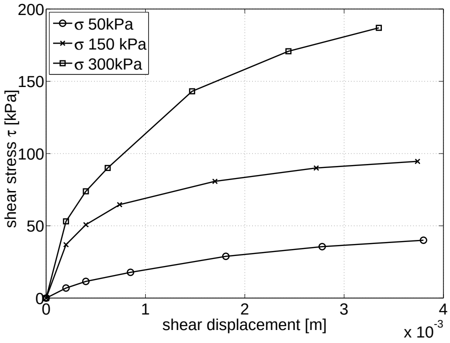

Figure 2.6: *direct shear test results.*

2.2 Tyre test

To include the tyre flexibility in the model, a modal analysis of the impulsive response of a real tyre has been carried out. The size of the considered tyre is 460/85R34, correspondng to 0.46 m of width and 0.8228 m of radius.

To infer the modal parameters from the impulsive response, the least square complex exponential method was used; this method works in time domain, presenting the advantage of not requiring an initial parameters estimate.

2.2.1 Impulsive test

The aim of the impulsive test was to identify the radial modes of the tyre, hence to measure the radial acceleration of the carcass 8 accelerometers were disposed regularly spaced around the carcass of the tyre, as shown in figure 2.7.

From literature results the modes shapes are expected to present an increasing number of lobes, as it is possible to infer from figure 2.8; since 8 measuring points do not allow to identify more than 4 nodes, only modes up to the fifth one will be recostructed.

Two different inflation pressures have been considered during the impulsive test, since tractor tyres usually work at about 1.6bar when driving on road and at about 1.0bar during machinery operations; indeed lower inflation pressure allows to obtain less sinkage, but increases the wear [20], hence on road a larger inflation pressure is preferable.

The impulsive force has been supplied through a dynamometric ham-

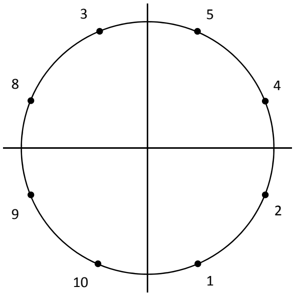

Figure 2.7: *Placement of the accelerometer sensors during the impulsive test of the tyre.*

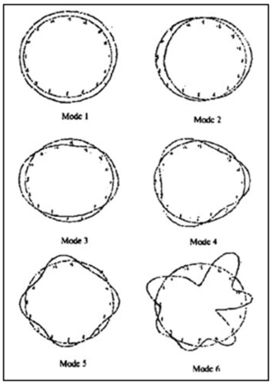
Mode 1
Mode 2
Mode 3
Mode 4
Mode 5
Mode 6

Figure 2.8: *expected modes shapes for cross-ply tyre [29]*

mer, whose cut-off frequency grows with the hammer load and the contact stiffness, as shown in figure 2.9.

Since it is possible to identify only up to the fifth mode with 8 accelerometers, the tyre can be hammered with a soft tip, corresponding to a cut out frequency of 100Hz. Furthermore the tyre was hammered near to a sensor, in order to measure the displacement of the forcing point.

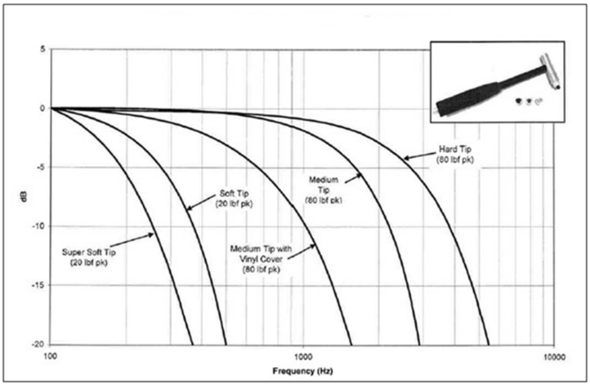

Figure 2.9: *filtering function of the hammer used to excite the tyre.*

In order to avoid the interferences in the measurement of the link system, the tyre was suspended at the center by a rigid link system, whose frequencies are higher than the range of interest. Moreover multiple test repetitions were carried out, so that the results could been filtered and averaged.

Thus the modal parameters were evaluated through the least square complex exponential method, as mentioned at the beginning of this section.

2.2.2 Least square exponential method

The least square exponential method allows to identify the parameters of the modes of a multi degrees of freedom system, without any initial extimation [24].

The starting point of this method is the receptance of frequency response function of the node j to an excitation in the node k, shown in equation 2.2. The parameters ω_r and $\omega_r^{'}$ are respectively the undamped and damped angular frequency of the r^{th} mode, ζ_r is the damping factor, which expresses the ratio between the damping of the r^{th} mode and the critical damping $2\sqrt{k_r m_r}$, and $r^{A_{jk}}$ is the amplitude of the r^{th} mode in the node j.

$$\alpha_{jk}\left(\omega\right) = \sum_{r=1}^{2N} \frac{r^{A_{jk}}}{\omega_r \zeta_r + i\left(\omega - \omega_r^{'}\right)} \tag{2.2}$$

$$\omega_r^{'} = \omega_r \sqrt{1-\zeta_r^2} \tag{2.3}$$

$$\omega_{r+N}^{'} = -\omega_r^{'} \tag{2.4}$$

$$(r+N)^{A_{jk}} = r^{A_{jk}^{*}} \tag{2.5}$$

By the inverse Fourier transform it is possible to obtain the impulse response function 2.6.

$$h_{jk}(t) = \sum_{r=1}^{2N} r^{A_{jk}} \omega_r e^{s_r t} \tag{2.6}$$

$$s_r = -\omega_r \zeta_r + i\omega_r^{'} \tag{2.7}$$

Since the original frequency response function has been obtained in a discrete form, the resulting impulse response function will similarly be described at a corresponding number of equally-spaced time intervals ($\Delta t = 1/\Delta f$), as in equation 2.8, where the subscripts jk have been omitted and A_r and $e^{s_r t}$ have been defined as in equation 2.9 and in equation 2.10 for the sake of simplicity.

$$h(t) = \sum_{r=1}^{2N} A_r V_r^l \tag{2.8}$$

$$A_r \doteq r^{A_{jk}} \tag{2.9}$$

$$e^{s_r t} \doteq V_r \tag{2.10}$$

By replicating the same procedure for the full data set of q sample, it is possible to obtain the equations systems 2.11.

$$\begin{array}{ccccccccc} h_0 & = & A_1 & + & A_2 & + & \ldots & + & A_{2N} \\ h_1 & = & V_1 A_1 & + & V_2 A_2 & + & \ldots & + & V_{2N} A_{2N} \\ h_2 & = & V_1^2 A_1 & + & V_2^2 A_2 & + & \ldots & + & V_{2N}^2 A_{2N} \\ \vdots & = & \vdots & & \vdots & & \vdots & & \vdots \\ h_q & = & V_1^q A_1 & + & V_2^q A_2 & + & \ldots & + & V_{2N}^q A_{2N} \end{array} \tag{2.11}$$

Provided that the number of sample q exceeds $4N$, where N is 5, the number of modes to reconstruct, this equation can be used to set up an eigenvalue problem, which solution supply the complex natural frequencies contained in the parameters V_l (for $l = 1 : 2N$) via a solution using the Prony method.

By multiplying each equation of the set 2.11 by a coefficient β_i, the equations systems 2.12 can be obtained.

$$\begin{array}{ccccccccc}
\beta_0 h_0 & = & \beta_0 A_1 & + & \beta_0 A_2 & + & \ldots & + & \beta_0 A_{2N} \\
\beta_1 h_1 & = & \beta_1 V_1 A_1 & + & \beta_1 V_2 A_2 & + & \ldots & + & \beta_1 V_{2N} A_{2N} \\
\beta_2 h_2 & = & \beta_2 V_1^2 A_1 & + & \beta_2 V_2^2 A_2 & + & \ldots & + & \beta_2 V_{2N}^2 A_{2N} \\
\vdots & = & \vdots & & \vdots & & \vdots & & \vdots \\
\beta_q h_q & = & \beta_q V_1^q A_1 & + & \beta_q V_2^q A_2 & + & \ldots & + & \beta_q V_{2N}^q A_{2N}
\end{array} \tag{2.12}$$

Adding all the equations of set 2.12 gives equation 2.13, where β_i are the coefficients of equations 2.14, whose roots are the parameters V_l.

$$\sum_{i=0}^{q} \beta_i h_i = \sum_{i=0}^{2N} A_j \left(\beta_i V_j^i\right) \tag{2.13}$$

$$\beta_0 + \beta_1 V + \beta_2 V^2 + \ldots + \beta_q V^q = 0 \tag{2.14}$$

Hence the system natural frequencies can be indentified solving the equation 2.14, once determined the coefficients β.

Considering $2N$ samples, from equation 2.14 it is possible to infer 2.15, thus every term on the right hand side of equation 2.13 is zeroed and it is possible to write equation 2.16.

$$\sum_{i=0}^{2N} \beta_i V_r^i = 0 \qquad \text{for } r = 1, 2 \tag{2.15}$$

$$\sum_{i=0}^{2N} \beta_i h_i = 0 \tag{2.16}$$

By setting $\beta_{2N} = 1$, it is possible to rearrange equation 2.16 as in 2.17.

$$\left\{ \begin{array}{cccc} h_0 & h_1 & \ldots & h_{2N-1} \end{array} \right\} \left\{ \begin{array}{c} \beta_0 \\ \beta_1 \\ \vdots \\ \beta_{2N-1} \end{array} \right\} = -h_{2N} \tag{2.17}$$

The entire process from equation 2.11 to equation 2.17 may be reapeated for another set of data points, further the new data set may overlap considerably the first set, as in equation 2.18.

$$\left\{ \begin{array}{cccc} h_0 & h_1 & \dots & h_{2N} \end{array} \right\} \left\{ \begin{array}{c} \beta_0 \\ \beta_1 \\ \vdots \\ \beta_{2N-1} \end{array} \right\} = -h_{2N+1} \tag{2.18}$$

Iteratively applying this procedure it is possible to obtain the equations set 2.19, whose solutions are the unknown coefficients β_i.

$$\left[\begin{array}{cccc} h_0 & h_1 & \dots & h_{2N-1} \\ h_0 & h_1 & \dots & h_{2N} \\ \vdots & \vdots & \ddots & \vdots \\ h_{2N-1} & h_{2N} & \dots & h_{4N-2} \end{array} \right] \left\{ \begin{array}{c} \beta_0 \\ \beta_1 \\ \vdots \\ \beta_{2N-1} \end{array} \right\} = - \left\{ \begin{array}{c} h_{2N} \\ h_{2N+1} \\ \vdots \\ h_{4N-1} \end{array} \right\} \tag{2.19}$$

Thus solving equation 2.14 it is possible to determine the values of V_1, $V_2, \dots, V_{2N}$, which let to identify the natural frequencies of the system by equation 2.10.

To complete the identification, the modal constants A_1, A_2, ... , A_{2N}, can be obtained by equation 2.11.

This method allowed to identify the modal shapes reported in figure 2.10, where it is possible to observe that the first mode corresponds to the expansion and contraction of the tyre carcass, the second mode is the displacement of the carcass with respect to the tyre center, whereas the third, fourth, and fifth mode correspond to carcass shape deformation, presenting respectively two, three and four lobes.

The inflation pressure exerts a high influence on the tyre dynamical response, determining the tyre stiffness, whereas poorly influences the modes shapes.

Table 2.2 shows the frequencies and damping factors of the modes previously described, as a function of the inflation pressure. When the tyre inflation is higher, the modes frequencies increase, on the contrary the damping factors decrease.

2.3 Traction test

To evaluate the traction performances of the tyre, whose mode had been identified, a traction test has been performed. This test allows to evaluate the traction force supplied by a tractor, where the testing tyres are mounted, as a function of the slippage.

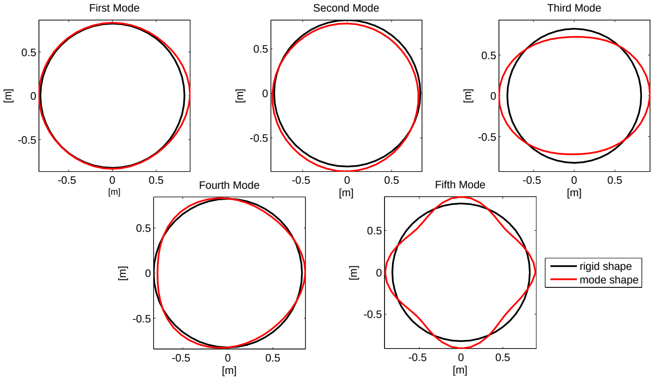

Figure 2.10: *shape of the modal deformates indentified*

Table 2.2: *parameters of the tyre structure*

	1.0 bar		1.6 bar	
Lobes number	Frequency [Hz]	Damp. factor [%]	Frequency [Hz]	Damp. factor [%]
0	11.2	5.8	11.8	5.8
1	26.5	4.4	27.1	4.6
2	39.3	3.1	42.4	3.6
3	46.3	1.3	51.9	2.8
4	56.3	6.0	62.2	5.8

To carry out this test two tractors were linked by a dynamometric bar, in order to measure the traction force provided by the front one as a function of the slip.

The testing tyres were mounted on the front tractor, and the rotational speed is measured by an encoder; whereas a free rolling wheel allows to measure the forward speed of the tractor, thus it is possible to infer the slip value, imposed by the rear tractor.

Figure 2.11 shows the traction force sustained by the driving tyres as a function of the slip, which varies in the range between 5 and 30%; it is possible to observe the traction force rises increasing the slip value.

The test was carried out with an inflation pressure of 1.0 bar, because it took place on a loose agricultural soil, where a low inflation pressure is preferred.

The data provided by this test will be used to validate the planar interac-

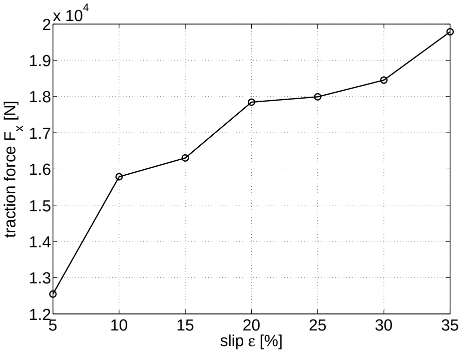

Figure 2.11: *Traction force available as a function of the slip on the tractive tyres*

tion model that will be presented in the next chapter (chap. 3).

Since the test evaluates the performances of the whole system composed by the tractor and the tyres, the simulation will be carried out taking into account the tractor properties, such as tractor load and the load transfer.

CHAPTER 3

Planar model

In this chapter a plane model of tyre-soil interaction will be presented: only the forces and displacements in vertical and longitudinal directions will be considered, whereas the lateral forces and diplacements will be neglected.

This planar model is specially designed to perform simulations of a tyre moving in longitudinal direction, paying particular attention to stationary conditions.

The model may be considered as consisting of two submodels interacting with each other: the tyre model and the soil model.

The soil is modeled by a layer of springs, which pressure on the tyre is proportional to the compression caused by the sinkage due to the tyre.

The tyre is modeled considering both the tread pattern geometry and the carcass flexibility. In first approximation the tyre deformation was neglected, since the soil one is markedly larger [28]. However the flexibility have been added, because of its influence on vibrations transmission and on interaction surface deformation.

Finally the results of some simulations carried out with the model will be discussed: firstly the validation of the model will be considered, thus a sensitivity analysis on the tread pattern geometry will be presented, and finally the results of simulations carried out with a whole tractor model will be shown, although these results were obtained with an earlier version of the model.

3.1 Tyre model

The tyre characteristics have a strong impact on the achievement of tractor requirements pointed out in the summary, hence the tyre model developed considers geometrical features of the tread pattern such as lugs heigh, orientation, and number, and dimension of the tyre such as width and radius, as well that structural properties, such as modes shape, frequency, and damping.

Indeed the geometry of the tread pattern determines the shape of the interaction surface between tyre and soil, whereas the tyre structural properties allow to consider the deformation of this interaction surface under the load and impact on the trasmission of force and acceleration to the hub.

The geometrical and structural properties of the tyre have been modeled by different features, that will be analysed in the next subsessions (3.1.1 and 3.1.2).

3.1.1 Tread pattern

For the sake of taking into account the influence of shape, number and height of the lugs, the geometry of the tread pattern has been modeled. The tread pattern is represented through four different surfaces, classified according to their position and orientation:

- BASE: the surface of the tip of the lugs.
- CEIL: the carcass surface among the lugs.
- FRONT: the surface of the side of the lugs, in particular the part of the lugs first entering in contact with the soil, according to the motion direction.
- REAR: the surface of the rear side of the lug, according to the motion direction.

Each of these surfaces interacts with the soil in a particular manner. Figure 3.1 shows a section of the tyre, where are marked the four surfaces and the normal and shear stresses references.

The normal stress σ is accounted to be positive when directed from the outer to the inner of the tyre, while the shear stress τ is accounted to be

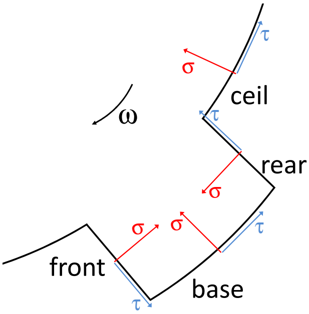

Figure 3.1: *the different orientation of the four surfaces modelling the tread pattern along a section of the tyre, and the references of normal and shear stresses.*

positive when oriented 90° clockwise with respect to the reference of the normal stress σ.

The base and ceil surfaces are normal to the radial direction, and their distances from the center of the tyre, where the hub is linked to the wheel, are respectively equal to the maximum and the minimum values of the tyre radius, whereas the front and rear surfaces are considered to lay on radial planes, thus their distance from the center is accounted for $R + h_{lug}/2$.

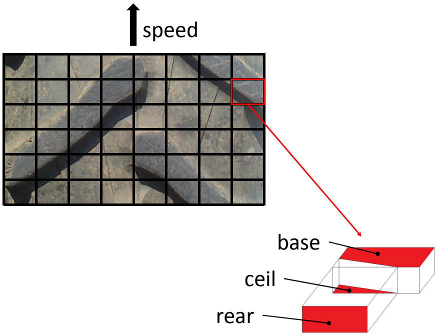

Figure 3.2: *the tread pattern has been divided by a grid, and each element of the grid has been associated with the areas covered by the four surfaces as shown for the element pointed out by way of example.*

If the tread pattern of figure 3.2 should be modeled, it would be gridded as shown in the same figure, and each element would be associate with the areas covered by the different surfaces. As an example an element is pointed out in figure 3.2. This element covers a part of the lug tip, corresponding to the base surface, a part of the lug rear side, corresponding to the rear surface, and a part of the carcass among the lugs, corresponding to the ceil surface; these three surfaces are marked in red, whereas the front surface is null because the front side of the lug is not included in the considered element.

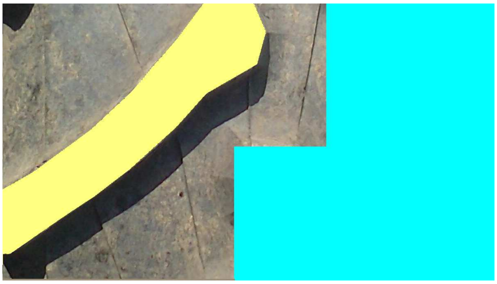

Figure 3.3: *The image of the tread pattern after preprocessing*

The surface identification allowing to build up the tread model is carried out by a code implemented in MATLAB language. The code works on an image of the tread pattern, where a lug is selected and the left part of the tread is masked as shown in figure 3.3; the code can recognize the shape of the lug and can infer its size with respect to the width of the tyre. Thus the whole tread can be built by mirroring and replicating the lug.

This procedure allows to build tread models with different numbers of lugs without modify the shape of the lug, indeed a different number of lugs can be placed on a tread of constant dimensions just by reducing or increasing the base surfaces among the lugs.

The forces experienced by each element of the carcass result from the stresses on each surfaces of the element and can be accounted as in equations 3.1 and 3.2, where the index k refers to the surface condidered (base, ceil, front or rear), and A_k is the area of that surface.

$$F_{\sigma,k} = \sigma_k A_k \tag{3.1}$$

$$F_{\tau,k} = \tau_k A_k \tag{3.2}$$

Hence at the center of the carcass the stress distribution on the carcass results in the forces F_x and F_z, respectively in longitudinal and vertical direction, and in the moment M_y around the lateral axis $\vec{y}$.

The forces F_x and F_z are accounted as in equations 3.3 and 3.4, where the index k and i refer respectively to the different surfaces and to the elements of the carcass, $\phi_{i,k}$ is the angle with the orizontal axis of the normal stress $\sigma_{i,k}$, and $A_{i,k}$ is the area covered by the surface k on the element i.

Instead the moment M_y depends on the distance from the center $d_{i,k}$ and on the stress in tangential direction $s_{i,k}$, which is the shear stress for base and ceil surfaces, and the normal stress for front and rear surfaces, as shown in equation 3.5.

$$F_x = \sum_{k=1}^{4} \sum_{i=1}^{N} \left[\sigma_{i,k} \cos\left(\phi_{i,k}\right) + \tau_{i,k} \cos\left(\phi_{i,k} - \frac{\pi}{2}\right)\right] A_{i,k} \tag{3.3}$$

$$F_z = \sum_{k=1}^{4} \sum_{i=1}^{N} \left[\sigma_{i,k} \sin\left(\phi_{i,k}\right) + \tau_{i,k} \sin\left(\phi_{i,k} - \frac{\pi}{2}\right)\right] A_{i,k} \tag{3.4}$$

$$M_y = \sum_{k=1}^{4} \sum_{i=1}^{N} s_{i,k}\, d_{i,k}\, A_{i,k} \tag{3.5}$$

These equations can be rewritten pointing out the contribution of each surface to the resulting force, as in 3.6, 3.7 and 3.8, indeed each surface is associated to different values of the variables $\phi_{i,k}$, $s_{i,k}$ and $d_{i,k}$.

$$F_x = F_{x,base} + F_{x,ceil} + F_{x,front} + F_{x,rear} \tag{3.6}$$

$$F_z = F_{z,base} + F_{z,ceil} + F_{z,front} + F_{z,rear} \tag{3.7}$$

$$M_y = M_{y,base} + M_{y,ceil} + M_{y,front} + M_{y,rear} \tag{3.8}$$

According to figure 3.1 the contribution of the different surfaces to the force F_x can be accounted as in equations 3.9, 3.10, 3.11 and 3.12, where θ_i is the central angle, accounted on counterclockwise direction, subtended by the element i.

$$\begin{aligned} F_{x,base} &= \sum_{i=1}^{N} \left[\sigma_{base} \cos\left(\theta_i + \pi\right) + \tau_{base} \cos\left(\theta_i + \frac{\pi}{2}\right)\right] A_{i,base} = \\ &= \sum_{i=1}^{N} \left[-\sigma_{base} \cos\left(\theta_i\right) - \tau_{base} \sin\left(\theta_i\right)\right] A_{i,base} \end{aligned} \tag{3.9}$$

$$F_{x,ceil} = \sum_{i=1}^{N} \left[\sigma_{ceil} \cos\left(\theta_i + \pi\right) + \tau_{ceil} \cos\left(\theta_i + \frac{\pi}{2}\right)\right] A_{i,ceil} =$$

$$= \sum_{i=1}^{N} \left[-\sigma_{ceil} \cos\left(\theta_i\right) - \tau_{ceil} \sin\left(\theta_i\right)\right] A_{i,ceil} \tag{3.10}$$

$$F_{x,front} = \sum_{i=1}^{N} h_{lug} \left[\sigma_{front} \cos\left(\theta_i + \frac{\pi}{2}\right) + \tau_{front} \cos\left(\theta_i\right)\right] =$$

$$= \sum_{i=1}^{N} h_{lug} \left[-\sigma_{front} \sin\left(\theta_i\right) + \tau_{front} \cos\left(\theta_i\right)\right] \tag{3.11}$$

$$F_{x,rear} = \sum_{i=1}^{N} h_{lug} \left[\sigma_{rear} \cos\left(\theta_i - \frac{\pi}{2}\right) + \tau_{rear} \cos\left(\theta_i - \pi\right)\right] =$$

$$= \sum_{i=1}^{N} h_{lug} \left[\sigma_{rear} \sin\left(\theta_i\right) - \tau_{rear} \cos\left(\theta_i\right)\right] \tag{3.12}$$

Similarly the contribution of the stresses on the carcass to the force F_z can be calculated as in equations 3.13, 3.14, 3.15 and 3.16.

$$F_{z,base} = \sum_{i=1}^{N} \left[\sigma_{base} \sin\left(\theta_i + \pi\right) + \tau_{base} \sin\left(\theta_i + \frac{\pi}{2}\right)\right] A_{i,base} =$$

$$= \sum_{i=1}^{N} \left[-\sigma_{base} \sin\left(\theta_i\right) + \tau_{base} \cos\left(\theta_i\right)\right] A_{i,base} \tag{3.13}$$

$$F_{z,ceil} = \sum_{i=1}^{N} \left[\sigma_{ceil} \sin\left(\theta_i + \pi\right) + \tau_{ceil} \sin\left(\theta_i + \frac{\pi}{2}\right)\right] A_{i,ceil} =$$

$$= \sum_{i=1}^{N} \left[-\sigma_{ceil} \sin\left(\theta_i\right) + \tau_{ceil} \cos\left(\theta_i\right)\right] A_{i,ceil} \tag{3.14}$$

$$F_{z,front} = \sum_{i=1}^{N} h_{lug} \left[\sigma_{front} \sin\left(\theta_i - \frac{\pi}{2}\right) + \tau_{front} \sin\left(\theta_i\right)\right] =$$

$$= \sum_{i=1}^{N} h_{lug} \left[\sigma_{front} \cos\left(\theta_i\right) + \tau_{front} \sin\left(\theta_i\right)\right] \tag{3.15}$$

$$F_{z,rear} = \sum_{i=1}^{N} h_{lug} \left[\sigma_{rear} \sin\left(\theta_i - \frac{\pi}{2}\right) + \tau_{rear} \sin\left(\theta_i - \pi\right)\right] =$$

$$= \sum_{i=1}^{N} h_{lug} \left[-\sigma_{rear} \cos\left(\theta_i\right) - \tau_{rear} \sin\left(\theta_i\right) \right] \tag{3.16}$$

The contribution of the stress on each surface to the moment M_y can be accounted as in equations 3.17, 3.18, 3.19 and 3.20, where R and h_{lug} are respectively the tyre radius and the heigh of the lugs, and are accounted for the distance of the application point of the resulting forces on the element.

$$M_{y,base} = \sum_{i=1}^{N} \tau_{base} A_{i,base} \left(R + h_{lug}\right) \tag{3.17}$$

$$M_{y,ceil} = \sum_{i=1}^{N} \tau_{ceil} A_{i,ceil}\, R \tag{3.18}$$

$$M_{y,front} = \sum_{i=1}^{N} \sigma_{front} A_{i,front} \left(R + \frac{h_{lug}}{2}\right) \tag{3.19}$$

$$M_{y,rear} = -\sum_{i=1}^{N} \sigma_{rear} A_{i,rear} \left(R + \frac{h_{lug}}{2}\right) \tag{3.20}$$

Moreover this model can take into account the partial sinkage of the lug, since the forces result from the calculation of the stress distributed only over the sinked part.

3.1.2 Tyre structure

Although the tyre flexibility is quite smaller than the soil one [28], the dynamic behaviour of the tyre plays an important role determining the shape of the interaction surface between the tyre and the soil and the vibration transmission from the interaction surface itself to the hub, hence it has been considered in the tyre model.

The model focuses on stationary conditions, hence the forward speed $\dot{x}$ and the slip ε (defined as in equation 3.21) are constant and set in simulation data; thus the tyre structure model describes the dynamics of the tyre in the vertical plane.

$$\varepsilon = \frac{\omega R - \dot{x}}{\omega R} \tag{3.21}$$

The tyre is assumed to be put on a tractor and, according to the weight distribution, part of the total mass of the tractor is assigned to the tyre hub, as shown in figure 3.4. Longitudinal speed of the hub and tyre slip are imposed, i.e. longitudinal displacement and rotation of the hub are regarded as constrained variables and the tyre hub presents 1 single degree of freedom (d.o.f.) represented by its vertical displacement.

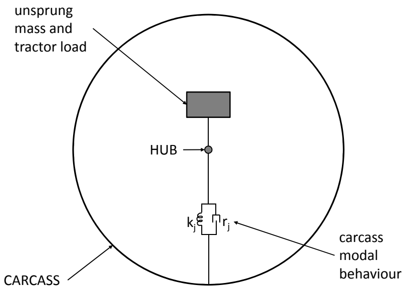

Figure 3.4: *scheme of the tyre structure model*

The flexibility of the tyre carcass is reproduced by means of a modal superposition approach. The motion equation for the tyre structure thus can be written as in eq. 3.22.

The first line of the system corresponds to the vertical displacement of the hub, whereas the next lines correpond to the model coordinates of the radial deformation. The mass m_{hub} collects the unsprung mass and the load of the tractor according to the weight distribution, whereas m_j, r_j, k_j represent respectively the modal mass, the equivalent damping and stiffness of the modal coordinate q_j.

The variables Q_{hub} and Q_j represent the modal forces acting on the center of the hub and on the modal coordinate q_j.

The hub is considered rigidly linked to the center of the tread carcass, hence the forces at the hub are directly inferred from the forces at the center of the tread carcass.

$$\begin{bmatrix} m_{hub} & & & \\ & m_1 & & \\ & & \ddots & \\ & & & m_n \end{bmatrix} \begin{Bmatrix} \ddot{z}_{hub} \\ \ddot{q}_1 \\ \vdots \\ \ddot{q}_n \end{Bmatrix} + \begin{bmatrix} 0 & & & \\ & r_1 & & \\ & & \ddots & \\ & & & r_n \end{bmatrix} \begin{Bmatrix} \dot{z}_{hub} \\ \dot{q}_1 \\ \vdots \\ \dot{q}_n \end{Bmatrix}$$

$$+\begin{bmatrix} 0 & & & \\ & k_1 & & \\ & & \ddots & \\ & & & k_n \end{bmatrix} \begin{Bmatrix} z_{hub} \\ q_1 \\ \vdots \\ q_n \end{Bmatrix} = \begin{Bmatrix} Q_{hub} \\ Q_1 \\ \vdots \\ Q_n \end{Bmatrix} \tag{3.22}$$

The modal forces are accounted from the external forces $\{F\}$ applied on the carcass nodes, as in equation 3.23; the jacobian matrix $[\Lambda]$ results from the modal identification and transforms the forces from the physical coordinates to the modal coordinates reference.

$$\{Q\} = [\Lambda] \{F (z_{hub}, q_1 \dots q_n)\} \tag{3.23}$$

The coupling among the different degrees of freedom of the system is performed by the external forces, since the modal coordinates determine the radius variation along the circumference, affecting both the sinkage of the carcass nodes, related to the normal stress, and the slippage, related to the shear stress, as it will be explained in section 3.3.

Indeed the variation of the radius along the circumference of the tyre can be determined from the modal coordinates, as shown in equation 3.24, where $\{r\}$ represents the vector of the distances from the center of the carcass nodes whereas R_0 the initial value of the radius.

$$\{r\} = [\Lambda]^T \{q\} + R_0 \tag{3.24}$$

The jacobian matrix of the eigenvectors $[\Lambda]$ has been derived through modal analysis of impulsive test, as explained in chapter 2; with the experimental test the modes in the range 10 and 60 Hz have been identified.

3.2 Soil model

The soil is modeled as a plane surface, whose nodes can move in vertical direction.

The soil reacts to the sinkage and to the slippage of the tyre with a normal and a shear stress on the carcass of the tyre. For the normal stress the Bekker theory have been accounted, although is has been linearized and modified to take into account the soil recovery, instead the calculation of the shear stress is based on the results on the experimental direct shear test presented in chapter 2.

3.2.1 Normal stress

The soil model is made up of a layer of springs whose compression, caused by the sinkage of the tyre, gives rise to a normal contact stress: the stress is assumed to be hydrostatic, i.e. even though sinkage is computed along a vertical axis, the resulting pressure acts along three directions [10] [28].

The relation between sinkage and normal stress depends on the time history of the deformation of the terrain. Indeed if the soil have already been compressed, its stiffness increases due to the compaction of the soil particles, hence the tyre experiences different conditions in the front and rear part of the contact track. Moreover the model can take into account the multipass effect, i.e. a tyre passing over a soil where previously another one rided works in different conditions than the first tyre.

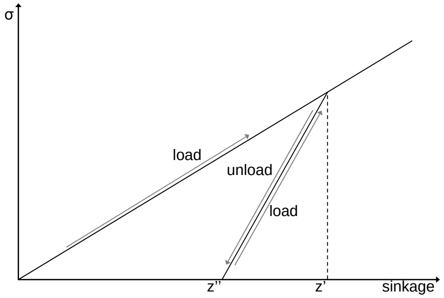

Figure 3.5: *normal stress as a function of the sinkage: assuming that a soil has been compressed at $z^{'}$, the unload phase from $z^{'}$ to $z^{''}$ and further load phases back to $z^{'}$ are described through a different linear relation whose slope K_{II} is higher than K_I*

This feature is explained in figure 3.5, where the relationship between the normal stress and the sinkage is drafted.

In initial conditions the soil sinkage and the normal stress are null and, when the load is applied the normal stress increases linearly with the sinkage, until sinkage $z^{'}$ is reached, when the load starts to decrease or is removed, thus the sinkage and the normal pressure decrease, but the soil stiffned, hence when the pressure is zeroed there is a residual sinkage $z^{''}$.

Then if the soil is newly compressed and pressure and sinkage rise, when the sinkage $z^{'}$ is reached, the soil stiffness decreases back to the initial value.

The results of the penetrometer test presented in chapter 2 have been accounted for the calculation of the initial stiffness K_I, which is the inverse of slope of the curve in figure 2.2 between 0 and 0.15 m, the sinkage range of interest for this application.

The stiffnes K_{II} has been calculated from maximum and residual sinkage $z^{'}$ and z$^{''}$, measured during experimental test, according to equation 3.25, which can been inferred from figure 3.5.

$$K_I z^{'} = K_{II}\left(z^{'} - z^{''}\right) \rightarrow K_{II} = K_I \frac{z^{'}}{z^{'} - z^{''}} \tag{3.25}$$

3.2.2 Shear stress

The shear stress is mainly affected by the shear displacement and the normal pressure, as seen in chapter 2.

Increasing the normal pressure, the maximum value of shear stress sustainable by the soil rises, as defined by the well known Mohr-Coulomb equation (eq. 3.26), where k_c and ϕ are respectively the cohesion and the free angle of shearing resistance of the soil, as mentioned in section 1.1.2.

$$\tau_{\max} = \left[k_c + \sin\left(\phi\right)\sigma\right] \tag{3.26}$$

Furthermore the shear stress is proportional to the shear displacement between the surface of the soil, which is supposed adhere to the tyre, and the deeper layers of the soil. That displacement at the instant t_i can be calculated as in equation 3.27, where $v_{slip,k}$ is the slip velocity on the surface k (base, ceil, front or rear) of the element i.

$$x_{slip,i,k}^{t_i} = v_{slip,i,k}^{t_i}\Delta t + x_{slip,i,k}^{t_{i-1}} \tag{3.27}$$

The slip velocity $v_{slip,k}$ depends on the vertical and longitudinal speeds of the center of the tyre, $\dot{z}$ and $\dot{x}$, on the tangential speed of the tyre ωR, on the velocity of tyre deformation $\dot{r}$, and on the surface orientation, as shown in figure 3.6.

Figure 3.6 shows the reference of the slip velocity according to the surface orientation: the slip velocity is positive when rotate of 90° in counterclockwise direction with respect to the normal direction entering in the surface, hence when the slip velocity is positive, also the shear stress is positive, according with its reference which is in the opposite direction.

To calculate the slip velocity, the equations 3.28, 3.29, 3.30 and 3.31 have been inferred from figure 3.6 and implemented in the model.

$$v_{slip,i,base} \;=\; \omega\left(R + h_{lug}\right) + \dot{x}\cos\left(\theta_i + \frac{\pi}{2}\right) + \dot{z}\cos\left(\pi - \theta_i\right)$$

$$
\begin{aligned}
&= \omega\left(R+h_{lug}\right)+\dot{x}\sin\left(\theta_i\right)-\dot{z}\cos\left(\theta_i\right) && (3.28)\\
v_{slip,i,ceil} &= \omega R+\dot{x}\cos\left(\theta_i+\frac{\pi}{2}\right)+\dot{z}\cos\left(\pi-\theta_i\right) &&\\
&= \omega R+\dot{x}\sin\left(\theta_i\right)-\dot{z}\cos\left(\theta_i\right) && (3.29)\\
v_{slip,i,front} &= \dot{x}\cos\left(\pi-\theta_i\right)+\dot{z}\cos\left(\frac{3\pi}{2}-\theta_i\right)-\dot{r} &&\\
&= -\dot{x}\cos\left(\theta_i\right)-\dot{z}\sin\left(\theta_i\right)-\dot{r} && (3.30)\\
v_{slip,i,rear} &= \dot{x}\cos\left(2\pi-\theta_i\right)+\dot{z}\cos\left(\frac{\pi}{2}-\theta_i\right)+\dot{r} &&\\
&= \dot{x}\cos\left(\theta_i\right)+\dot{z}\sin\left(\theta_i\right)+\dot{r} && (3.31)
\end{aligned}
$$

To infer the relationship between the shear displacement and the shear stress on the carcass, a direct shear test has been carried out on a soil sample [6]; thus the analytical relationship of equation 3.32 has been stated to fit the experimental data.

$$
\tau_{i,k}=\left(c_1\sigma_{i,k}+c_2\right)\sqrt{x_{slip}}+\left(c_3\sigma_{i,k}+c_4\right)\sqrt[3]{x_{slip}}+c_5\sigma_{i,k}^2+c_6\sigma \qquad (3.32)
$$

This equation allows to determine the shear stress as a function of both the shear displacement and the normal stress, unlike the Mohr-Coulomb equation 3.26, which point out only the value of the maximum shear stress sustainable by the soil $\tau_{\max}$.

Figure 3.7 shows the fitting of the experimental results provided by the equation 3.32, whose parameter are shown in table 3.1: the test has been carried out for three different values of the normal pressure: respectively 100 kPa, 150 kPa and 300 kPa.

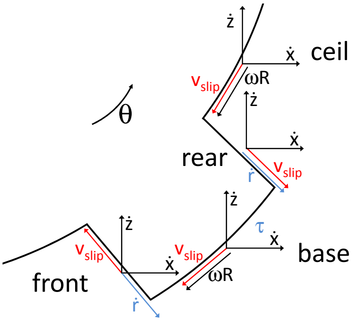

Figure 3.6: *the slip velocity reference and component depending on the surface orientation.*

Table 3.1: *parameters of the equation 3.32 interpolating the direct shear test results*

Parameter		Value
c_1	$[\mathrm{m}^{-\frac{1}{2}}]$	6.412
c_2	$[\mathrm{kPa}\cdot\mathrm{m}^{-\frac{1}{2}}]$	-262.816
c_3	$[\mathrm{m}^{-\frac{1}{3}}]$	1.698
c_4	$[\mathrm{kPa}\cdot\mathrm{m}^{-\frac{1}{3}}]$	137.486
c_5	$[\mathrm{kPa}^{-1}]$	$5.646 \cdot 10^{-6}$
c_6	[]	$-6.457 \cdot 10^{-3}$

From the experimental results it is possible to verify that a rise of normal pressure increases the shear stress, because the larger compaction of soil particles has a favorable effect on soil shear resistance.

The results have been extrapoled in order to be used in all the interest domain, as shown in figure 3.8.

Moreover the maximum allowed shear displacement depends on the slip value, since an increase in slip involves a rise of slip velocity reducing the maximum shear displacement susteinable by the soil.

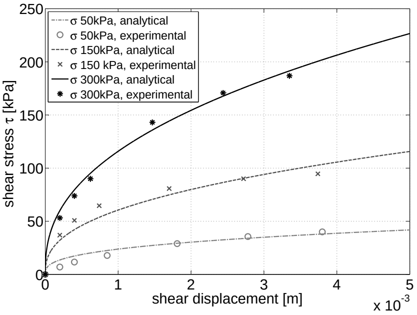

Figure 3.7: *the shear stress is a function of the shear stress and of the pressure: the experimental results have been interpooled with analytical expression.*

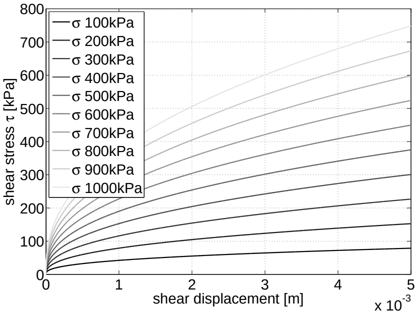

Figure 3.8: *the shear stress is a function of the shear stress and of the pressure: increasing pressure and displcement, the shear stress increases.*

3.3 Tyre-soil interaction

The interaction between the tyre and the soil provides the forces on the tread, which determine the generalized forces Q_{hub} and Q_j acting on the system d.o.f., as in equation 3.22.

The calculation has been performed according to the scheme of figure

3.9, where it is depicted the absolute position of point $C_{i,k}$, the geometrical center of the k-th area ($A_{i,k}$) of the i-th element of the grid (see figure 3.1); since each element is characterized by four surfaces (ceil, base, front, rear), k varies between 1 and 4.

Futhermore figure 3.9 reports also the position of the tyre hub (point O) and the distance between $C_{i,k}$ and O, named $r_{i,k}$. If point $C_{i,k}$ finds below the undeformed soil level, it will be characterized by a sinkage $s_{i,k}$.

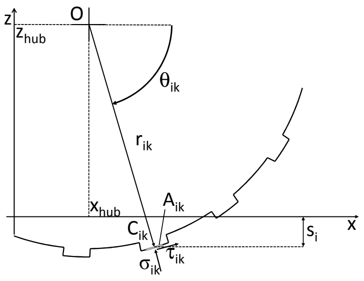

Figure 3.9: *position of the center of the k^{th} area of the i^{th} element of the grid*

The absolute position of $C_{i,k}$ can be computed as follows in equation 3.33, where θ_i is the certral angle subtended by the i^{th} element.

$$\left\{\begin{array}{lcl} x_{C_{i,k}} & = & x_{hub} + r_{i,k}\cos\left(\theta_i\right) \\ z_{C_{i,k}} & = & z_{hub} - r_{i,k}\sin\left(\theta_i\right) \end{array}\right. \tag{3.33}$$

Considering the flexibility of the tyre structure, the radius R_{ik} will be function of the modal coordinates, according to the expression 3.34.

$$\left\{\begin{array}{lcl} x_{C_{i,k}} & = & x_{hub} + \left[R_0 + \Sigma_{j=1}^{N}\left(\Lambda_{i,k,j}\cdot q_j\right)\right]\cos\left(\theta_i\right) \\ z_{C_{i,k}} & = & z_{hub} - \left[R_0 + \Sigma_{j=1}^{N}\left(\Lambda_{i,k,j}\cdot q_j\right)\right]\sin\left(\theta_i\right) \end{array}\right. \tag{3.34}$$

Indeed the coordinates of the point $C_{i,k}$ can be calculated by adding the projection of the radius to the coordinates of the hub.

Since the radial flexibility has been considered, the modal coordinates q_j are accounted for the radius variation, hence, in equation 3.34 of the term $\Lambda_{ik,j}$ is the element of j^{th} eigenvector corresponding to the location of $C_{i,k}$.

Considering the vertical position of $C_{i,k}$, it is possible to compute the sinkage $s_{i,k}$ and the value of the contact pressure $\sigma_{i,k}$ acting on the k^{th} area of the i^{th} element. According to the procedure described in the previous paragraph, the value of the tangential stress $\tau_{i,k}$ can also be found. The virtual work of the external forces acting on the k^{th} area of the i^{th} element is given by equation 3.35, where $m_{i,k}$ is the mass associated with the k^{th} area of the i^{th} element.

$$\begin{aligned}\delta L_{i,k} = & \left\{-m_{i,k}g + \left[\sigma_{i,k}\sin\left(\theta_i\right) - \tau_{i,k}\cos\left(\theta_i\right)\right]A_{i,k}\right\}\delta z_{C_{i,k}} - \\ & - \left[\sigma_{i,k}\cos\left(\theta_i\right) + \tau_{i,k}\sin\left(\theta_i\right)\right]A_{i,k}\delta x_{C_{i,k}}\end{aligned} \tag{3.35}$$

Substituting equation 3.34 in equation 3.35, the virtual work can be expressed as in equation 3.36.

$$\begin{aligned}\delta L_{ik} = & \left\{-m_{ik}g + \left[\sigma_{ik}\sin\left(\theta_{ik}\right) - \tau_{ik}\cos\left(\theta_{ik}\right)\right]A_{ik}\right\} \\ & \left\{\delta z_{hub} + \Sigma_{j=1}^{N}\left[\Lambda_{ik,j}\cdot q_j\sin\left(\theta_{ik}\right)\right]\right\} - \\ & - \left[\sigma_{ik}\cos\left(\theta_{ik}\right) + \tau_{ik}\sin\left(\theta_{ik}\right)\right]A_{ik} \\ & \left\{\delta x_{hub} + \Sigma_{j=1}^{N}\left[\Lambda_{ik,j}\cdot q_j\cos\left(\theta_{ik}\right)\right]\right\}\end{aligned} \tag{3.36}$$

Considering also the mass of the hub itself, the value of the forces reduced at vertical displacement of the tyre hub is represented by equation 3.37.

$$\begin{aligned}Q_{hub} = & - m_{hub}g - \Sigma_{i=1}^{N_{el}}\left\{\Sigma_{k=1}^{4}\left(m_{i,k}g\right)\right\} - \\ & - \Sigma_{i=1}^{N_{el}}\left\{\Sigma_{k=1}^{4}\left[\sigma_{i,k}\sin\left(\theta_i\right) - \tau_{i,k}\cos\left(\theta_i\right)\right]\right\}\end{aligned} \tag{3.37}$$

Also the value of Q_j can be derived as in equation 3.38.

$$\begin{aligned}Q_{hub} = & \Sigma_{i=1}^{N_{el}}\left\{\Sigma_{k=1}^{4}\left(\Lambda_{i,k,j}\sin\left(\theta_{i,k}\right)m_{i,k}g\right)\right\} - \\ & -\Sigma_{i=1}^{N_{el}}\left\{\Sigma_{k=1}^{4}\left[\sigma_{i,k}\sin\left(\theta_i\right) - \tau_{i,k}\cos\left(\theta_i\right)\right]A_{ik}\Lambda_{i,k,j}\sin\left(\theta_i\right)\right\} + \\ & +\Sigma_{i=1}^{N_{el}}\left\{\Sigma_{k=1}^{4}\left[\sigma_{i,k}\cos\left(\theta_i\right) - \tau_{i,k}\sin\left(\theta_i\right)\right]A_{i,k}\Lambda_{i,k,j}\sin\left(\theta_i\right)\right\}\end{aligned} \tag{3.38}$$

Since $\sigma_{i,k}$, and thus $\tau_{i,k}$, are function of the sinkage, which is itself function of both the vertical displacement of the hub and of the modal coordinates, the motion equation are coupled by the contact forces.

3.4 Model validation

The model has been validated by comparison with the results of an experimental traction test, which has been presented in section 2.3.

The traction force supplied by the tractor was halved, since during the experimental test the traction were provided by two tyres, whereas in the simulations only one tyre is modeled.

Futhermore during the experimental test the rolling resistance on the front tyres contributes to the traction force, whereas during the simulations this contribution can not be accounted since the front tyre has not been modeled. However the front tyres contribution to the total forces is lower than the one of the rear tyres, due to the load distribution, which is preponderant on the rear axle sustaining almost the 65% of the total tractor load. Moreover, the rolling resistance is much lower than the traction force sustained by the driving tyres.

Hence neglecting the rolling resistance on the front tyre should introduce an overestimation of the traction supplied by the rear tyre, which can be estimated to be lower than 10% of the total force.

Figure 3.10 shows the traction force available at a driving tyre as a function of the slip, which varies in the range 5-30%.

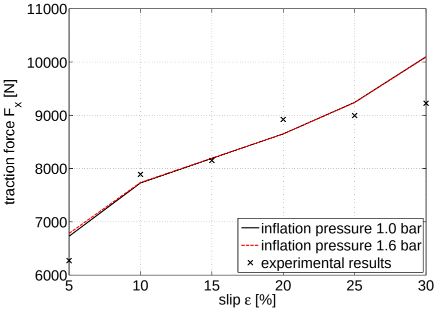

Figure 3.10: *traction force available as a function of slip and of inflation pressure*

The traction force rises increasing the slip value, and it is possible to observe that the results of the model are in good agreement with the experimental results, guaranteeing an error less than 3% between 10% and 25% of slip as shown in table 3.2.

The test was carried out with an inflation pressure of 1.0 bar, because it was performed on an agricultural soil, where a low inflation pressure is preferred.

Whereas the simulations where carried out considering both low inflation pressure (1.0 bar) and high inflation pressure (1.6 bar): the inflation pressure has not great impact on the traction force, affecting instead the interaction surface shape, thus the maximum sinkage (see figure 3.11) and the

Table 3.2: *comparison between numerical and experimental results of a traction test*

Slip value [%]	Experimental results Force [N]	Numerical results Force [N]	Error [%]
5	6273	6730	7.3
10	7892	7730	2.1
15	8152	8190	0.5
20	8922	8651	3.0
25	8996	9243	2.8
30	9226	10099	9.5

standard deviation of the vertical acceleration of the hub (see figure 3.12).

As it can be inferred from figure 3.11, the soil sinkage rises increasing the slip value, since to perform a larger traction force the lugs grab and dig the soil.

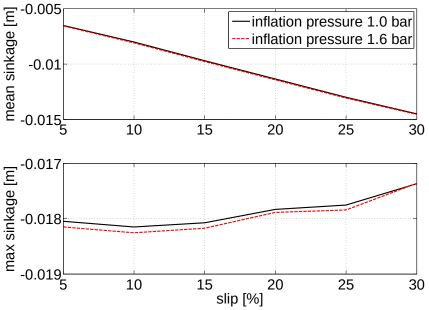

Figure 3.11: *soil sinkage as a function of slip and of inflation pressure.*

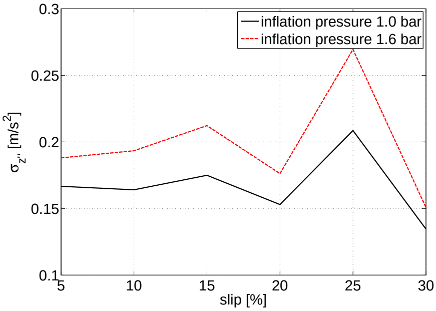

Figure 3.12: *standard deviation of the hub vertical acceleration as a function of slip and of inflation pressure.*

The comfort can be inferred from the vertical acceleration of the hub (figure 3.12); thus it is possible to state that the low inflated tyre can guarantee higher comfort level.

Moreover it is possible to observe a peak at the 25% of the slip, indeed at this slip value the impact frequency of the lugs excite one of the tyre modes.

3.5 Pattern sensitivity analysis

The presented model can take into account different tread patterns, hence it can be an useful tool to perform a sensitivity analysis.

In this section a sensitivity analysis on the paramenter of a tread pattern will be performed. In particular the tread pattern of figure 3.13 will be considered, which is a tipical tread for traction tyres [47].

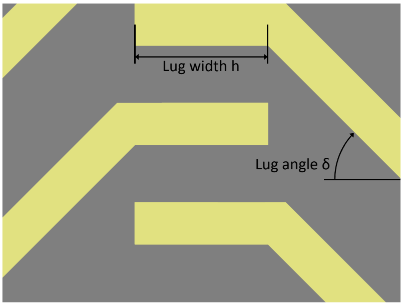

Figure 3.13: *tread pattern modulus*

The length h and the angle δ of the lugs were varied on order to find the optimus configuration: the reference length and angle are respectively 80 mm and 45°and the effect of a variation of ±10% and ±20% will be accounted, as shown table 3.3.

Table 3.3: *variation of the tread pattern parameters*

Parameter	-20%	-10%	0%	+10%	+20%
h [mm]	64	72	80	88	96
δ [°]	25	35	45	55	65

The aim of this sensitivity analysis was to point out the better configuration for a driving tyre working on a loose soil, thus the simulations parameters correspond to this situation.

A slow forward speed and two different slip values have been considered: the forward speed is 7 km/h, which is a typical speed over field, and the selected slip values are 5%, corresponding to riding without machinery, and 25%, typical of machinery operations, such as tillage.

The inflation pressure of the tyres is 1.0 bar, preferred on loose soils in order to reduce sinkage and soil compaction.

The tyre is suppposted to be mounted on a tractor of mean size. The load on the tyre is 1390 kg and the wheelbase is 2770 mm.

3.5.1 Traction force

Figures from 3.14 to 3.23 show the influence of lugs length and inclination on tyre traction force: the lugs inclination is marked on the x-axis, while the bars refer to different lugs number.

Figures 3.14, 3.16, 3.18, 3.20, and 3.22 refer to simulations with 5%, whereas figures 3.15, 3.17, 3.19, 3.21, and 3.23 refer to simulations with 25% of slip.

Each pair of figures pertains to a different length of the central part of the lugs, from shorter (64 mm) in figure 3.14 and 3.15 to longer (96 mm) in figure 3.22 and 3.23.

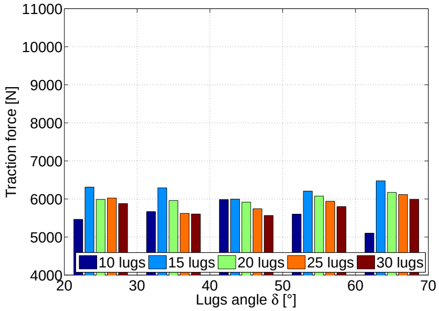

Figure 3.14: *traction force as a function of lugs number and angle, for center length of 64 mm and 5% of slip*

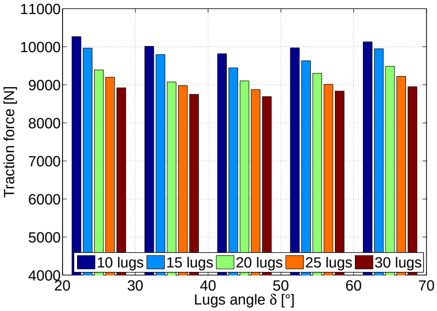

Figure 3.15: *traction force as a function of lugs number and angle, for center length of 64 mm and 25% of slip*

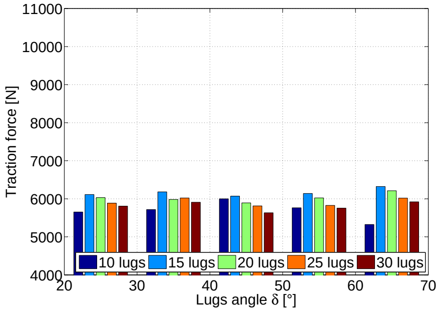

Figure 3.16: *traction force as a function of lugs number and angle, for center length of 72 mm and 5% of slip*

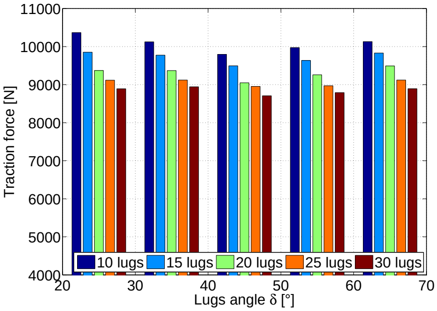

Figure 3.17: *traction force as a function of lugs number and angle, for center length of 72 mm and 25% of slip*

With regard to the lugs number, it is possible to observe that the maximum traction force is found for 15 lugs at 5% slip, whereas at 25% slip the maximum corresponds to 10 lugs.

The front side of the lugs supplies an important fraction of the traction force, hence a low lugs number can not guarantee an elevate traction force,

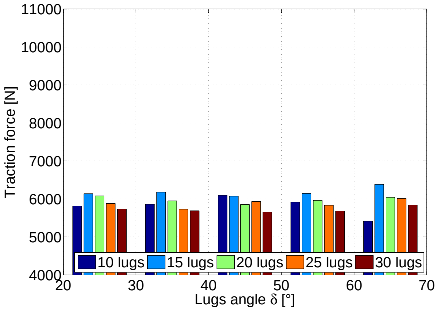

Figure 3.18: *traction force as a function of lugs number and angle, for center length of 80 mm and 5% of slip*

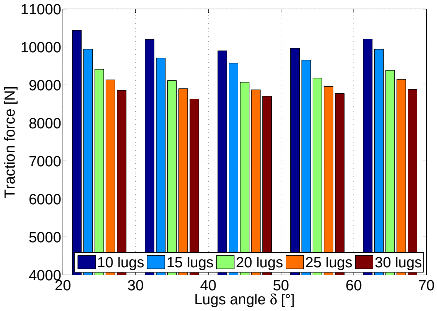

Figure 3.19: *traction force as a function of lugs number and angle, for center length of 80 mm and 25% of slip*

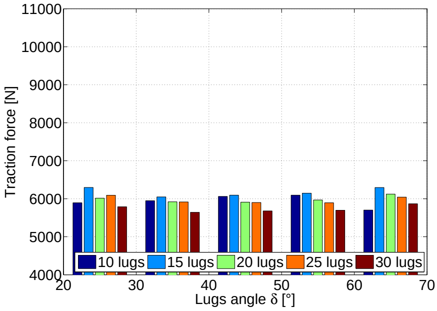

Figure 3.20: *traction force as a function of lugs number and angle, for center length of 88 mm and 5% of slip*

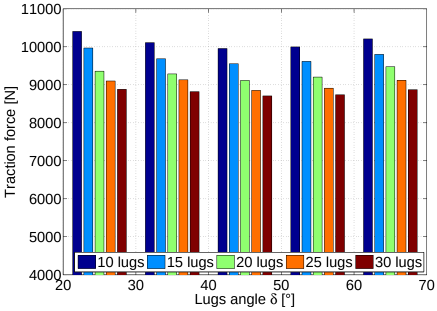

Figure 3.21: *traction force as a function of lugs number and angle, for center length of 88 mm and 25% of slip*

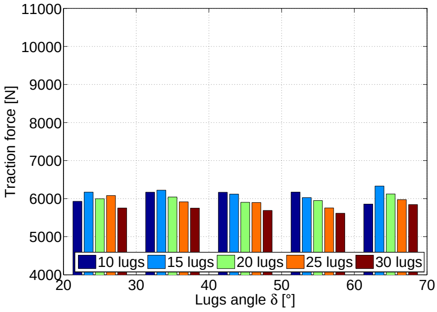

Figure 3.22: *traction force as a function of lugs number and angle, for center length of 96 mm and 5% of slip*

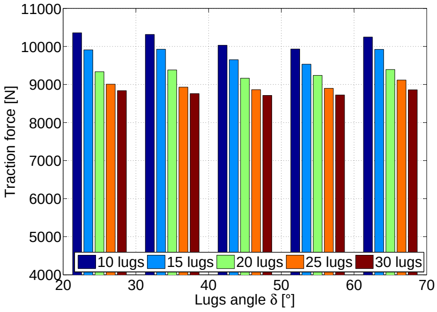

Figure 3.23: *traction force as a function of lugs number and angle, for center length of 96 mm and 25% of slip*

whereas a high lugs number tends to uniform the tread surface and the lugs can not perform a high traction force.

Increasing the slip value, the first lugs dig out the soil and the next lugs have not soil to grab, hence at a slip value of 25% the number of lugs corresponding to the maximum value of the traction force is lower than at a slip value of 5%.

The lugs angle and length have no significant effect on the traction force, although it is possible to observe a little increase in traction force for high inclination angle.

However the configuration with 45°of inclination is usually preferred, because it guarantee a better stability against the lateral forces [47], which are not accounted in this model, since it considers only forces and acceleration in the vertical plane.

3.5.2 Standard deviation of the hub acceleration

Figures from 3.24 to 3.33 show the influence of lugs length and inclination on the standard deviation of the vertical acceleration of the hub.

As in subsection 3.5.1 the lugs inclination is marked on the x-axis, while the bars refer to different lugs number and each pair of figures pertains to a different length of the central part of the lugs, from shorter (64 mm) in figure 3.24 and 3.25 to longer (96 mm) in figure 3.32 and 3.33.

Figures 3.24, 3.26, 3.28, 3.30, and 3.32 refer to simulations with 5%, whereas figures 3.25, 3.27, 3.29, 3.31, and 3.33 refer to simulations with 25% of slip.

The vertical acceleration of the hub is an important variable, moreover since the driver seat is not model, can be accounted fot the comfort estimate.

From these figures it is possible to observe that the three parameters considered have a strong impact on vertical acceleration.

As regard the lugs number, it is possible to notice a minimum in the standard deviation of the vertical acceleration at 15 lugs. Indeed a low lugs number can not supply a continuous sustain to traction and vertical forces, whereas a high lugs number involves a large number of lug impacts with the soil, thus affecting negatively the vibrations level.

Instead as regard the lugs length h it is possible to observe a significant rise of the vibrations level when the length of the central part of the lug increases. Indeed the central part of the lugs comes into contact with the soil contemporary, causing an increase of the vibrations, whereas the angled part of the lugs supply a more gradual contact with the soil. Thus increasing the size of the straight part of the lugs with respect to the angled

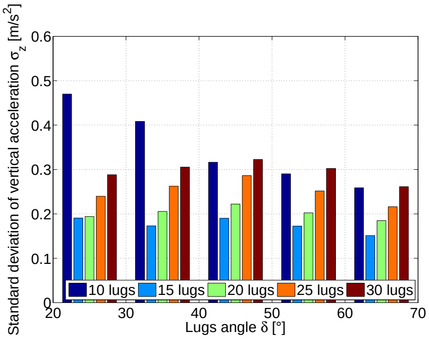

Figure 3.24: *standard deviation of the hub vertical acceleration σ_z as a function of lugs number and angle, for center length of 64 mm and 5% of slip*

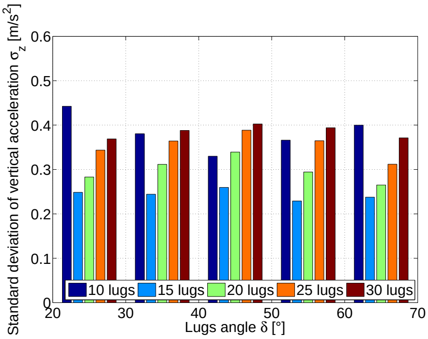

Figure 3.25: *standard deviation of the hub vertical acceleration σ_z as a function of lugs number and angle, for center length of 64 mm and 25% of slip*

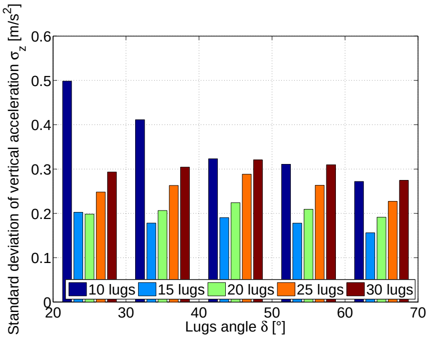

Figure 3.26: *standard deviation of the hub vertical acceleration σ_z as a function of lugs number and angle, for center length of 72 mm and 5% of slip*

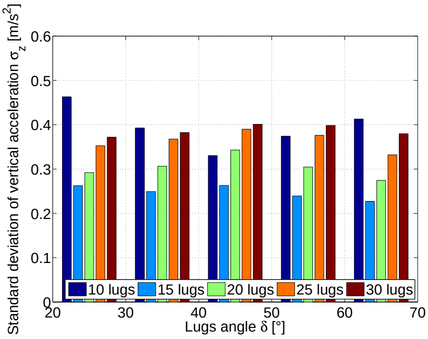

Figure 3.27: *standard deviation of the hub vertical acceleration σ_z as a function of lugs number and angle, for center length of 72 mm and 25% of slip*

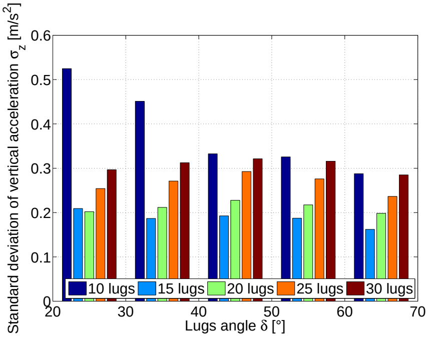

Figure 3.28: *standard deviation of the hub vertical acceleration* σ_z *as a function of lugs number and angle, for center length of 80 mm and 5% of slip*

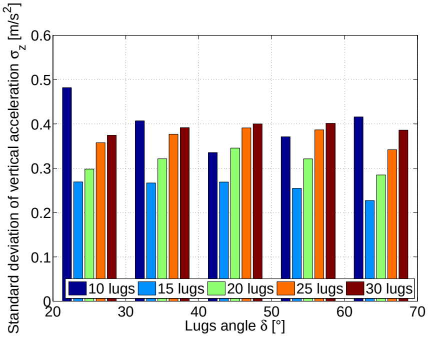

Figure 3.29: *standard deviation of the hub vertical acceleration* σ_z *as a function of lugs number and angle, for center length of 80 mm and 25% of slip*

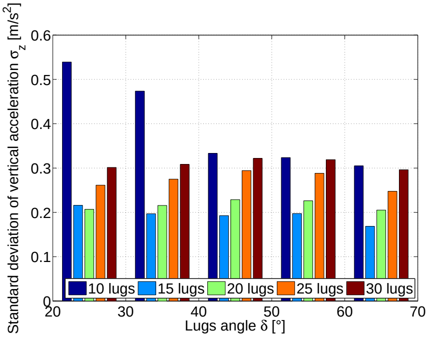

Figure 3.30: *standard deviation of the hub vertical acceleration* σ_z *as a function of lugs number and angle, for center length of 88 mm and 5% of slip*

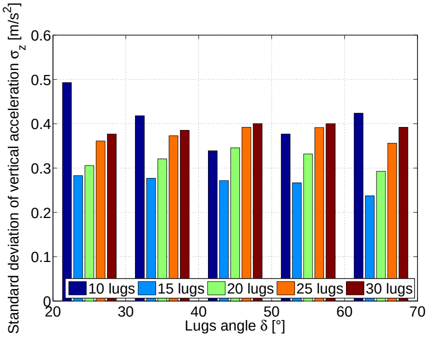

Figure 3.31: *standard deviation of the hub vertical acceleration* σ_z *as a function of lugs number and angle, for center length of 88 mm and 25% of slip*

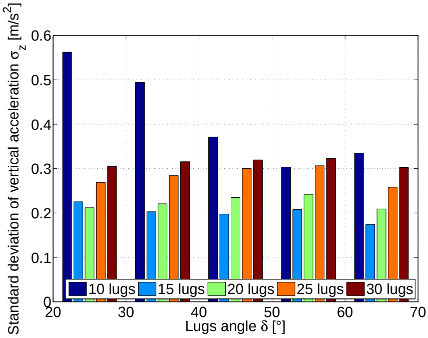

Figure 3.32: *standard deviation of the hub vertical acceleration σ_z as a function of lugs number and angle, for center length of 96 mm and 5% of slip*

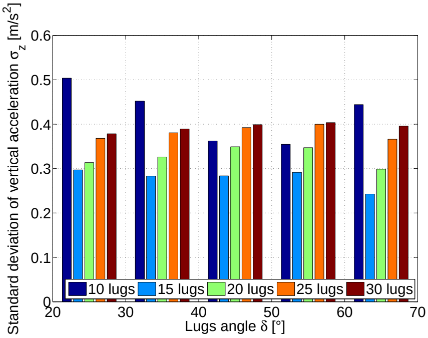

Figure 3.33: *standard deviation of the hub vertical acceleration σ_z as a function of lugs number and angle, for center length of 96 mm and 25% of slip*

one involves a rise of acceleration standard deviation.

For the same reason a higher lugs angle δ corresponds to lower vibrations level.

It is also possible to notice a relevant impact of the slip value on the standard deviation of the hub vertical acceleration: increasing the slip value the standard deviation rises, since it is excited by the lugs impact on the soil.

3.5.3 Sinkage

Figures from 3.34 to 3.43 show the influence of lugs length and inclination on the maximum sinkage of the soil after the tyre pass, which can be accounted for an index of the soil compaction level.

As previously in subsections 3.5.1 and 3.5.2, the lugs inclination is marked on the x-axis, while the bars refer to different lugs number and each pair of figures pertains to a different length of the central part of the lugs, from shorter (64 mm) in figure 3.34 and 3.35 to longer (96 mm) in figure 3.42 and 3.43.

In figures 3.34-3.43 it is noticeable the influence of the lugs number, whereas the lugs length h, the lugs angle δ and the slip value do not affect markedly the maximum sinkage of the soil.

The maximum sinkage is due to the lugs tips, since for a lager lugs number there is a larger surface suppling the vertical load, thus a lower sinkage is required.

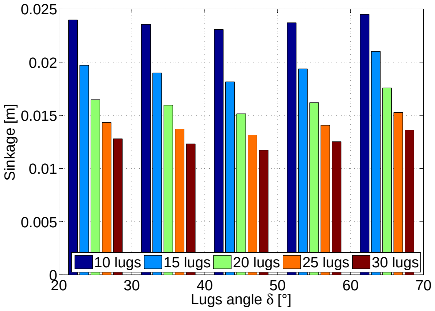

Figure 3.34: *maximum sinkage as a function of lugs number and angle, for center length of 64 mm and 5% of slip*

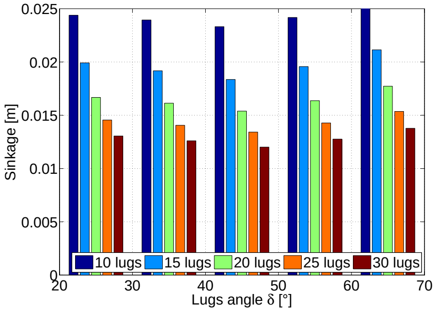

Figure 3.35: *maximum sinkage as a function of lugs number and angle, for center length of 64 mm and 25% of slip*

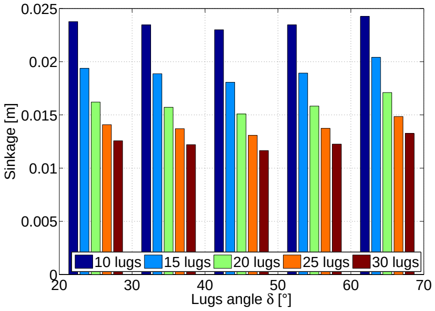

Figure 3.36: *maximum sinkage as a function of lugs number and angle, for center length of 72 mm and 5% of slip*

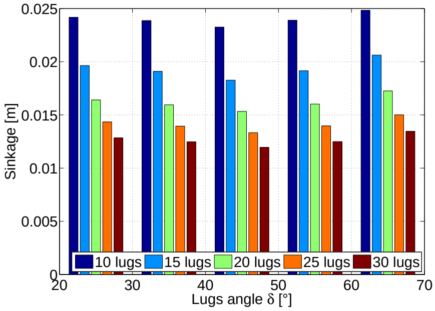

Figure 3.37: *maximum sinkage as a function of lugs number and angle, for center length of 72 mm and 25% of slip*

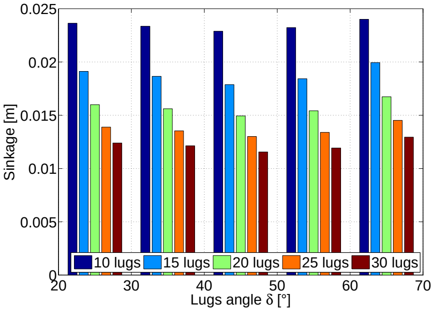

Figure 3.38: *maximum sinkage as a function of lugs number and angle, for center length of 80 mm and 5% of slip*

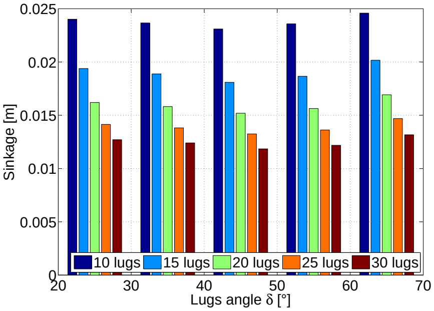

Figure 3.39: *maximum sinkage as a function of lugs number and angle, for center length of 80 mm and 25% of slip*

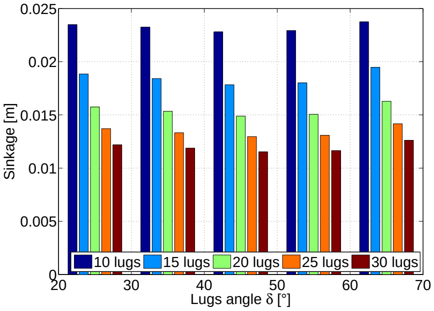

Figure 3.40: *maximum sinkage as a function of lugs number and angle, for center length of 88 mm and 5% of slip*

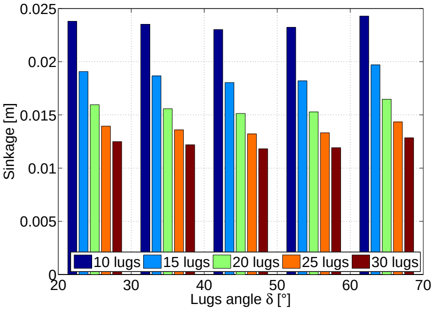

Figure 3.41: *maximum sinkage as a function of lugs number and angle, for center length of 88 mm and 25% of slip*

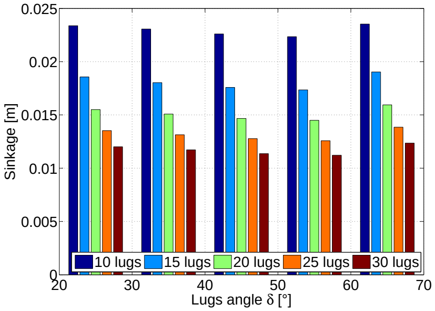

Figure 3.42: *maximum sinkage as a function of lugs number and angle, for center length of 96 mm and 5% of slip*

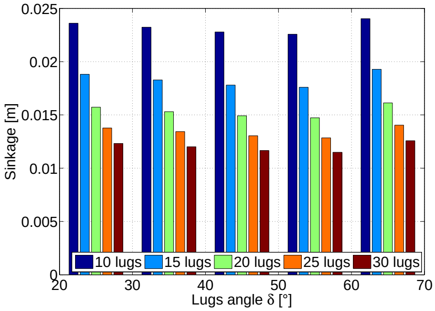

Figure 3.43: *maximum sinkage as a function of lugs number and angle, for center length of 96 mm and 25% of slip*

3.5.4 Sensitivity analysis conclusions

These simulations showed the capability of the developed code to carry out a sensitivity analysis taking into account the main features of the tread pattern geometry.

In particular, for this tread shape, it has been possible to observe that the number of lugs corresponding to the maximum value of the traction force is affected by the slip value, however a low lugs number can be recommended. A low standard deviation of vertical acceleration is achieved with 15 lugs, whereas to avoid a deep sinkage a high lugs number is recommended. Hence to satisfy all the requirements in tyre performances, i.e. to perform high traction force at low vibrations level and minimal sinkage, 20 lugs can be recommended, to mix the best performances of high and low lugs number.

As regards the lugs length h and angle δ a short lug and a high inclination can be recommended to reduce the vibrations, despite these results were obtained neglecting the lateral forces, whose vibrations can be reduced at 45°lugs angle [47].

3.6 Whole tractor model

The model stated in the previous sections (3.1.1-3.3) may simply interact with a multi-body model of a tractor.

The position, velocity and acceleration of the center of the carcass are imposed to the hub, which is linked rigidly or by means of suspensions to the tractor frame. Similarly the forces are transmitted from the frame to the tyre and vice versa.

The model of the whole tractor dynamics allowed to study the driver comfort as a function of suspensions damping, as shown in [15] and in [48].

The results provided in this section were performed with an early model of the tyre, that considered only the vertical displacement of the carcass with respect to the center of the tyre, corresponding to the second mode of the five identificated in section 2.2.

3.6.1 Tractor multi-body model

The modeled agricultural vehicle is the high-range tractor shown in figure 3.44.

The vehicle can be considered as composed by three rigid bodies, connected each other by means of suspensions.

- The frame, where are placed the engine and the cabin.
- The cabin.
- The seat.

A pneumatic spring and a damper connect the seat with the cabin, which is itself connected to the frame by means of three passive pneumatic suspensions (air springs).

The front tyres are joint to the frame by means of actively controllable double wishbone suspensions, that can support two working conditions: during field operations (tilling, ground compaction, etc.), the actuators can be locked up (the suspension is thus rigid), whereas, when the vehicle is running on ordinary roads, the actuators can be unlocked in order to damp the vehicle pitch. The suspension can be manually switched on or off by the operator. On the contrary, no suspensions are present between the rear axle and the frame.

Figure 3.45 shows a sketch of the multi-body model of the tractor:

- One rigid body represents the vehicle frame having three d.o.f. (heave, pitch and roll); besides this body includes all the elements rigidly linked to the frame, such as the engine and the rear axle.
- One rigid body represents the cabin, having three d.o.f. (heave, pitch and roll);
- Two rigid bodies representing the front unsprung masses, each one having one d.o.f. (heave). If the front suspensions are locked up, these bodies are gathered in the frame body.

- Two rigid bodies having each one vertical d.o.f, represent the seat and the load mounted on it which simulates the equivalent mass of the operator.

The model's parameters, shown in table 3.4, were identified by a comparison with the results of a four-poster test bench previously carried out on a four-post test rig, as it will be explain in the next section (sec. 3.6.2).

Table 3.4: *stiffness and damping of the tractor model*

Visco-elastic element		Stiffness [N/m]	Damping [N/m·s]
Frame Suspensions	Front	320000	40000
	Rear	-	-
Cabin Suspensions	Front	73724	6000
	Rear	73724	6000
Seat Suspensions	-	5840	624
Tyre	Front	628470	4902.1
	Rear	874390	5602.4

3.6.2 Tractor multi-body model validation

The implemented vehicle model shown in the previous section (sec. 3.6.1) has been validated by means of the comparison with a experimental tests, which were previously carried out on the vehicle shown in figure 3.44 on a four-post test rig.

The vehicle was instrumented to measure the accelerations of its different components.

The three accelerations of the cabin and its pitch, roll and yaw angular

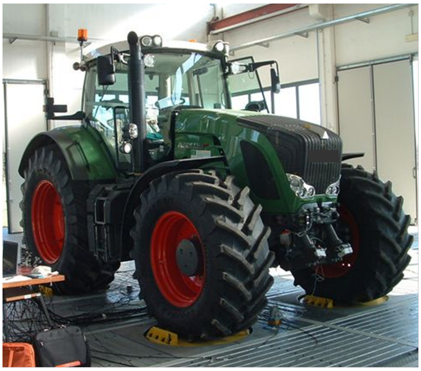

Figure 3.44: *tested vehicle on the four-post test rig.*

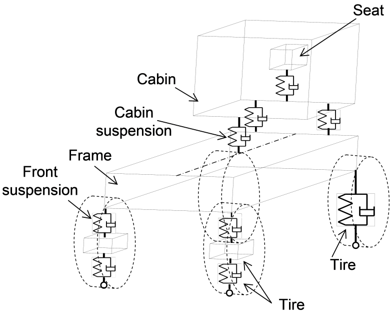

Figure 3.45: *multi-body vehicle model*

rates were measured by an inertial gyroscopic platform. The accelerations on the back and on the plane of the driver seat were measured through two tri-axial piezoelectric accelerometers. Whereas the frames accelerations were measured by mean of four piezo-accelerometers at the corners of the vehicle frame.

Tests have been performed measuring the vehicle response to the excitation of pads chirp signals (sweep sine tests), transmitted by the four-post test rig [14, 17].

Sweep sine tests have been carried out in order to excite the vehicle eigenmodes of heave, roll and pitch separately: to excite the vertical motion of the vehicle, the four actuators of the test-rig have been moved in phase, to evaluate the pitch motion the rear actuators were moved in counter phase with respect of the front ones, and finally to excite the roll motion the right actuators were moved in counter phase with respect of the left ones.

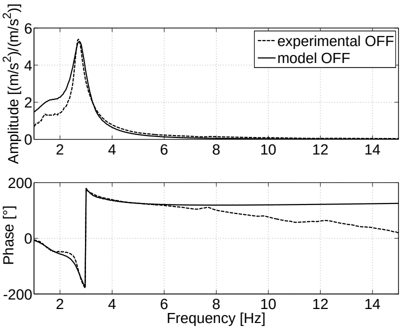

Figure 3.46: *cabin heave accelerations during a sweep sine test with all the actuators moved in phase. Front suspension switched off.*

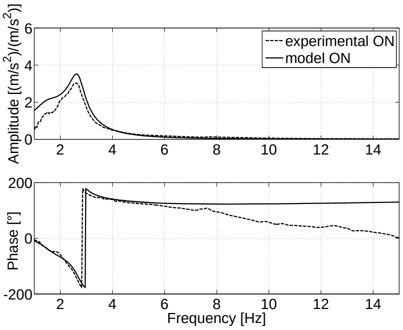

Figure 3.47: *cabin heave accelerations during a sweep sine test with all the actuators moved in phase. Front suspension switched on.*

Tests have been repeated considering different excitation amplitudes, and with the front suspension switched off and on.

As an example of the obtained results, the transfert functions of the acceleration response of the cabin to the excitation of the heave and pitch motion will be presented.

Figures 3.46 and 3.47 refer to a sweep sine test with all the actuators moved in phase, thus exciting the heave mode, respectively with the front suspensions locked and unlocked. The cabin vertical acceleration shows a main peak at a frequency of 3Hz, which reduces its amplitude unlocking the front suspesions.

Figures 3.48 and 3.49 refer to a sweep sine test with all the front actua-

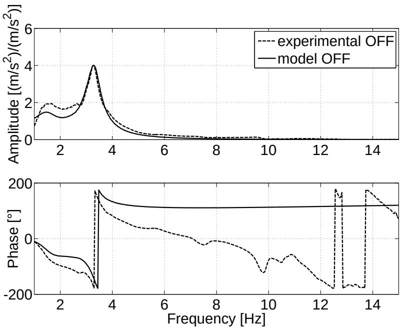

Figure 3.48: *cabin pitch accelerations during a sweep sine test with front and rear actuators moved in counter phase. Front suspension switched off.*

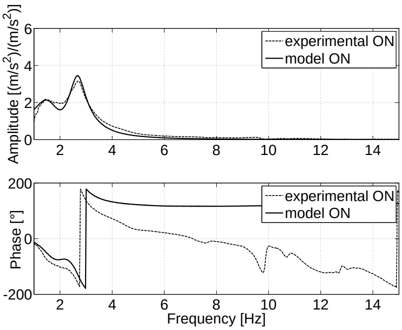

Figure 3.49: *cabin pitch accelerations during a sweep sine test with front and rear actuators moved in counter phase. Front suspension switched on.*

tors moved in counter phase with respect to the rear ones, thus exciting the pitch mode, respectively with the front suspensions locked and unlocked. The cabin pitch acceleration shows a main peak at a frequency of 4Hz and a lower peak at a frequency of 2Hz. Unlock the front suspensions reduces the amplitude of peak at 4Hz.

From the observation of these figures, a good agreement can be noticed between the experimental and the numerical results, for both amplitude and phase of the transfer functions.

3.6.3 Tractor multi-body model simulation

In this sections some of the results obtained with the soil-tyre interaction model linked to the multi-body model of the tractor will be discussed.

The simulations were performed with a tyre of size 540/65R28, with 20 lugs per side, whose shape can be observed in the image of the tread pattern of figure 3.50.

As previously observed (see 3.6), these simulation were carried out with an early model of the tyre structure, that considered only the mode corresponding to the vertical displacement of the center of the carcass with respect of the hub. Table 3.5 shows the structural properties of the tyres, as they were identified from the test presented in section 3.6.2; front and rear tyres present different properties, associated to different dimensions of the tested tyres, although in the presented simulations the front and rear tyres have the same size.

The simulations were performed over a North Gower Sandy loam soil,

Table 3.5: *stiffness and damping of the tyres*

Tyre	Mass [kg]	Stiffness [N/m]	Damping [N/m·s]
Front	67	628470	4902.1
Rear	67	874390	5602.4

whose properties are shown in table 3.6.

These properties refers to Bekker and Mohr Coulomb equations (see section 1.1), whose parameters as a function of the soil type are available in litterature.

These parameters were used to state the relationship between the soil stresses and displacements in an early version of the model, when the experimental results presented in section 2.1 were not available, as explained in [18] and [19].

Table 3.6: *North Gower sandy loam soil properties*

Bekker parameters			Mohr-Coulomb parameters	
k_c [kPa·m^{1-n}]	k_ϕ [kPa·m^{-n}]	n [-]	$k_{cohesion}$ [kPa]	ϕ [%]
41.6	24.71	0.73	6.1	26.6

Figures 3.51 and 3.52 show some of the results that have been obtained with this model.

In figure 3.51 the soil deformation after the tractor passage is depicted. It is possible to discern the tracks of the front tyres from the track of the rear ones, since the sinkage due to the front tyres is lower than the one related to the rear tyres, because of the weight distribution. Moreover it is possible

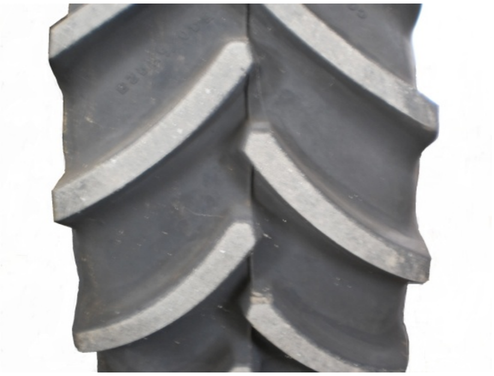

Figure 3.50: *tread pattern of the tyre modeled for the simulations performed considering the interaction with a multi-body model of the whole tractor*

to notice where the tractor stopped when the simulation ended, indeed in correspondence of the tyres there is no elastic recovery of the soil and the sinkage is deeper.

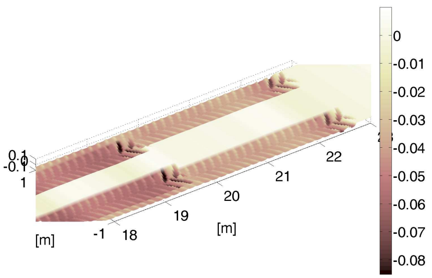

Figure 3.51: *soil deformation after the tractor passage*

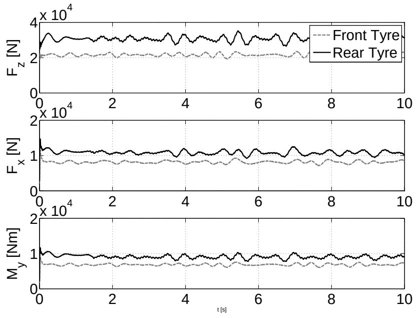

Figure 3.52: *interaction forces between the soil and the tyre*

Figure 3.52 shows the forces due to the interaction with the soil experienced at the hubs of the tractor. The figure refers to the left tyres, since the forces are equally distributed on the left and right side of the tractor, because of the symmetry of the model and of the initial smoothness of the soil.

In this simulations all the wheels were driving, hence also the front tyres contribute to the traction force, that can be computed as in equation 3.39, where the pairs of subscripted indexes refer to the tyre position (e.g. FR means front right tyre).

$$\begin{aligned} F_{traction} &= F_{x,FR} + F_{x,FL} + F_{x,RR} + F_{x,RL} + \\ &= 2F_{x,FL} + 2F_{x,RL} \end{aligned} \tag{3.39}$$

The presented model were stated to perform an evaluation of the driver comfort, since it considers the vertical dynamics of the whole vehicle. Thus some results on the standard deviation of the vertical acceleration at the driver seat will be presented.

Figure 3.53 shows the standard deviation of the vertical acceleration of the driver seat as a function of cabin damping R$_c$; the different lines refer to different values of the seat damping.

Is is possible to observe that the optimal parameters values, that can be inferred from the figure, perform a comfort level pretty similar to the one guaranteed by the nominal values of the these parameters, which are 624 N/m·s for the seat damping and 6000 N/m·s for the cabin one.

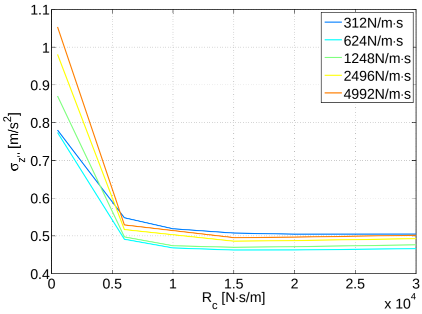

Figure 3.53: *standard deviation of the vertical acceleration of the driver seat as a function of cabin and seat damping*

3.7 Conclusions

In this chapter a planar model for the tyre-soil interaction has been presented.

This model takes into account the effect of tread pattern geometry and tyre structure, hence it can perform simulations aimed to study the influence of soil and tyre parameters on traction force, driver comfort, and soil sinkage and compaction.

Moreover this model may interact with the multi-body model of a whole tractor, providing a tool for the study of the tyre influence on tractor dynamics.

However this model can not take into account build up or cleaning effect, which impact on traction efficiency and soil compaction, thus in the next chapter a particles model will be presented, that is intended to provide more accurate soil model.

CHAPTER 4

Particle Model

The plane model that has been presented in the previous chapter (see chapter 3) considers the soil as a plane surface, whose nodes can move vertically under the tyre yield.

That plane model allows to study the interaction between the soil and the tyre, pointing out the effects of that interaction on forces, vibrations and topsoil deformation; nevertheless that model cannot provide results on compaction and deformation of the subsoil, moreover by modelling the soil as a continuous surface it is no possible to take into account effects affecting the tyre performances, like buildup and cleaning, consisting respectively in the buildup of matter in front of the tyre and in soil particles adhering to the tread pattern.

To face these issues a multi-body approach was introduced: the soil is modeled through a particles set, presenting different dimensions and properties, and moving relative to one another.

This chapter will be devoted to describe the tridimensional particle model proposed with the purpose of study the tyre soil interaction. This model is based on the Chrono::Engine multi-body library, developed by UniversitÃ di Parma and Wisconsin University.

To face the large amount of bodies needed to represent the soil, the code run on graphic processing unit (GPU) [36].

The approach of this multi-body library is based on differential variational intequalities (DVI) [2], as it will be discussed in the next section .

4.1 Differential Variational Inequalities

4.1.1 Problem formulation

The formulation of the equations of motion, that are the equations governing the time evolution of a multi-body system, is based on the Cartesian representation of the attitude of each rigid body of the system [36].

Suppose the system composed by n_b bodies, thus the attitude of the j^{th} body can be denoted by its rotation $\boldsymbol{\epsilon}_j$ and the center of gravity position $\mathbf{r}_j$. Hence the state of the system can be denoted by the generalized positions q and their derivative $\dot{\text{q}}$ as expressed in equations 4.1 and 4.2.

$$\mathbf{q} = \left\{\mathbf{r}_1^T, \boldsymbol{\epsilon}_1^T, \ldots, \mathbf{r}_{nb}^T, \boldsymbol{\epsilon}_{nb}^T\right\} \in \mathbb{R}^{7n_b} \tag{4.1}$$

$$\dot{\mathbf{q}} = \left\{\dot{\mathbf{r}}_1^T, \dot{\boldsymbol{\epsilon}}_1^T, \ldots, \dot{\mathbf{r}}_{nb}^T, \dot{\boldsymbol{\epsilon}}_{nb}^T\right\} \in \mathbb{R}^{7n_b} \tag{4.2}$$

To avoid singularities, the bodies rotations are expressed by quaternions, however it is more advantageous to use the angular velocities than the quaternion derivatives equation, so the system generalized velocities can be expressed as shown in equation 4.3.

$$\mathbf{v} = \left\{\dot{\mathbf{r}}_1^T, \overline{\boldsymbol{\omega}}_1^T, \ldots, \dot{\mathbf{r}}_{nb}^T, \overline{\boldsymbol{\omega}}_{nb}^T\right\} \in \mathbb{R}^{6n_b} \tag{4.3}$$

Anyway the generalized velocity can be easily obtained by a linear mapping transforming each $\overline{\omega}_i$ into the corresponding quaternion derivative $\dot{\epsilon}_i$, as show in equation 4.4, obtained by means of the linear algebra formula 4.5, defined according to Shabana [51].

$$\dot{\mathbf{q}} = \mathbf{L}\left(\mathbf{q}\right)\mathbf{v} \tag{4.4}$$

$$\dot{\epsilon}_i = \frac{1}{2}\mathbf{G}^T\left(\mathbf{q}\right)\overline{\omega}_i \tag{4.5}$$

The evolution of the multi-body system is governed by the second order differential equation 4.6, where M is the mass matrix, which remains constant and diagonal, since the system is composed by rigid bodies, and $\mathbf{f}^A\left(t, \mathbf{q}, \mathbf{v}\right)$ is the set of generalized external forces applied on the bodies.

$$\mathbf{M}\mathbf{v} = \mathbf{f}^A\left(t, \mathbf{q}, \mathbf{v}\right) \tag{4.6}$$

That notation does not take into account the presence of constrains, neither unilateral nor bilateral, which will be considered in the next section.

4.1.2 Constraints formulation

To accomplish the formulation of the problem, the constraints have to be accounted. In this section both bilateral and unilateral constrains will be discussed.

- Bilateral constrains represent kinematic pairs, such as spherical, prismatic and revolute joints, and constrain the relative position of two bodies. These constraints can be expressed by means of holonomic algebraic equations.
- Unilateral constrains gathering the contacts between two bodies, accounting for the presence of contact and friction forces.

Bilateral constraints

A set $\mathcal{B}$ of bilateral constrains generates a collection of scalar equations (eq. 4.7)

$$\boldsymbol{\Psi}_i\left(\mathbf{q},t\right)=0 \qquad i\in\mathcal{B} \tag{4.7}$$

Assuming smoothness of the constraint manifold, the equations collection $\boldsymbol{\Psi}_i$ can be differentiated to obtain the Jacobian matrix, as in equation 4.8.

$$\nabla_q\boldsymbol{\Psi}_i=\left[\frac{\partial\boldsymbol{\Psi}_i}{\partial\mathbf{q}}\right]^T \tag{4.8}$$

The bilateral constraints must be satisfaited also at the velocity level, hence the total time derivative of $\boldsymbol{\Psi}_i$ is null (eq. 4.9).

$$\begin{aligned}&\frac{d\boldsymbol{\Psi}_i\left(\mathbf{q},t\right)}{dt}=0 \qquad\qquad (4.9)\\&\Rightarrow\frac{\partial\boldsymbol{\Psi}_i}{\partial\mathbf{q}}\dot{\mathbf{q}}+\frac{\partial\boldsymbol{\Psi}_i}{\partial t}=\nabla_q\boldsymbol{\Psi}_i^T\dot{\mathbf{q}}+\frac{\partial\boldsymbol{\Psi}_i}{\partial t}=\nabla_q\boldsymbol{\Psi}_i^T\mathbf{L}\left(\mathbf{q}\right)\mathbf{v}+\frac{\partial\boldsymbol{\Psi}_i}{\partial t}=0\end{aligned}$$

Thus defining

$$\nabla\boldsymbol{\Psi}_i^T=\nabla_q\boldsymbol{\Psi}_i^T\mathbf{L} \tag{4.10}$$

the constraints are consistent at velocity-level, provided the equation 4.11 is satisfied. Note that the partial derivative of $\boldsymbol{\Psi}_i$ is non-zero only for rheonomic constrains, such as motors, actuators or imposed trajectory.

$$\nabla\boldsymbol{\Psi}_i^T\mathbf{v} + \frac{\partial\boldsymbol{\Psi}_i}{\partial t} = 0 \tag{4.11}$$

Unilateral constrains

A set of contact points among a large number of bodies can be defined efficiently by modern detection algorithms.

For each pair of contacts points a gap function $\Phi\left(\mathbf{q}\right)$ can be defined, expressing the distance between two bodies near enough.

Where defined, this gap function must satisfied the non-penetration condition 4.12, i.e. it must not be negative.

$$\Phi\left(\mathbf{q}\right) \geq 0 \tag{4.12}$$

The gap function is simple to define for smooth and convex bodies, such as spheres, parallelepipeds and cylinders. Hence the complex geometry profile of some bodies will be produced by decomposition in simple subshapes. With this assumption, any contact can be described by a contact function that is twice continuosly differentiable.

When the gap function is zeroed, the contact is active and a normal and a tangential force act on each of the two bodies in the contact point. For the calculation of these forces, the classical Coulomb friction model is accounted [1]. Whereas if the gap function is strictly positive, the bodies are not in contact and exchange no forces.

This condition leads to a complementarity problem [54].

Given two bodies A and B in contact, the normal direction at the contact point $\mathbf{n}_i$ is accounted toward the exterior of the body of lower index, let be body A.

The friction force is impressed by means of multipliers $\hat{\gamma}_{i,n}$,$\hat{\gamma}_{i,u}$ and $\hat{\gamma}_{i,w}$, leading to formulations 4.13 and 4.14 for normal and tangential force respectively.

$$\mathbf{f}_{i,N} = \hat{\gamma}_{i,n}\mathbf{n}_i \tag{4.13}$$

$$\mathbf{f}_{i,T} = \hat{\gamma}_{i,u}\mathbf{u}_i + \hat{\gamma}_{i,w}\mathbf{w}_i \tag{4.14}$$

Thus the Coulomb model for the friction forces lead to the non-linear constrains expressed in equation 4.15, where $\mathbf{v}_{i,T}$ represents the relative tangential velocity at the contact i.

$$\begin{aligned}
&\hat{\gamma}_{i,n} \geq 0, \qquad \mathbf{\Phi}_i\left(\mathbf{q}\right) \geq 0, \qquad \mathbf{\Phi}_i\left(\mathbf{q}\right)\hat{\gamma}_{i,n} = 0, \\
&\mu_i\hat{\gamma}_{i,n} \geq \sqrt{\hat{\gamma}_{i,u}^2 + \hat{\gamma}_{i,w}^2}, \quad \|\mathbf{v}\|\left(\mu_i\hat{\gamma}_{i,n} - \sqrt{\hat{\gamma}_{i,u}^2 + \hat{\gamma}_{i,w}^2}\right) = 0, \\
&\langle \mathbf{f}_{i,T}, \mathbf{v}_{i,T}\rangle = -\|f_{i,T}\|\|v_{i,T}\|
\end{aligned} \tag{4.15}$$

The operator $\langle\ ,\ \rangle$ defines the inner product of two vectors, hence the constrain $\langle \mathbf{f}_{i,T}, \mathbf{v}_{i,T}\rangle = -\|f_{i,T}\|\|v_{i,T}\|$ requires that the tangential force must be opposite to the tangential velocity. The friction coefficient is $\mu_i \in \mathbb{R}^+$; note that this model does not distinguish between static and kinetic coefficients, although it can be easily considered if necessary.

The first part of the constrain can be restated as in equation 4.16, where $\mathcal{Y}$ is a cone in three dimensions, whose slope is $\arctan\left(\mu_i\right)$.

$$\mathbf{f}_i = \mathbf{f}_{i,N} + \mathbf{f}_{i,T} = \hat{\gamma}_{i,n}\mathbf{n}_i + \hat{\gamma}_{i,u}\mathbf{u}_i + \hat{\gamma}_{i,w}\mathbf{w}_i \in \mathcal{Y} \tag{4.16}$$

Furthermore this constrain can be also reformulated considering the maximum dissipation principle, as in equation 4.17.

$$\left(\hat{\gamma}_{i,u}, \hat{\gamma}_{i,w}\right) = \underset{\sqrt{\hat{\gamma}_{i,u}^2 + \hat{\gamma}_{i,w}^2} \leq \mu_i\hat{\gamma}_{i,n}}{\text{argmin}} \ \mathbf{v}_{i,N}^T\left(\hat{\gamma}_{i,u}\mathbf{u}_i + \hat{\gamma}_{i,w}\mathbf{w}_i\right) \tag{4.17}$$

4.1.3 The overall model

Considering the constrain formulation in the dynamics equation 4.6 leads to the overall model.

At time t a set $\mathcal{A}$ of relevant contact constrains is active (eq. 4.18): in order to avoid wasting of computation effort in this set are considered only the pairs of bodies whose shapes are at a distance smaller than $\delta > 0$, touching, interpenetrating or separated.

$$\mathcal{A}\left(\mathbf{q}, \delta\right) = \left\{i | i \in \left\{1, 2, \ldots, p\right\}, \Phi\left(\mathbf{q}\right) \leq \delta\right\} \tag{4.18}$$

Moreover it is active a set $\mathcal{B}$ of bilateral contact; each one of these constraints transmits forces to the paired bodies by means of a multiplier $\hat{\gamma}_{i,b}$.

Considering these constraints, the overall model is denoted as in equation 4.19; the problem so defined is a differential problem with set-valued functions and complementarity constrains, which is equivalent to a differential variational inequality [45].

$$
\begin{aligned}
\dot{\mathbf{q}} &= \mathbf{L}\left(\mathbf{q}\right)\mathbf{v} \\
\mathbf{M}\mathbf{v} &= \mathbf{f}\left(t, \mathbf{q}, \mathbf{v}\right) + \\
&\quad + \sum_{i \in \mathcal{A}(\mathbf{q}, t)} \left(\hat{\gamma}_{i,n}\mathbf{D}_{i,n} + \hat{\gamma}_{i,u}\mathbf{D}_{i,u} + \hat{\gamma}_{i,w}\mathbf{D}_{i,w}\right) + \sum_{i \in \mathcal{B}} \hat{\gamma}_{i,b} \nabla \mathbf{\Psi}_i \\
& i \in \mathcal{B} : \mathbf{\Psi}\left(\mathbf{q}, t\right) = 0, \qquad (4.19) \\
& i \in \mathcal{A}\left(\mathbf{q}, \delta\right) : \hat{\gamma}_{i,n} \leq 0 \perp \mathbf{\Phi}\left(\mathbf{q}\right) \geq 0, \\
\left(\hat{\gamma}_{i,u}, \hat{\gamma}_{i,w}\right) &= \underset{\sqrt{\hat{\gamma}_{i,u}^2 + \hat{\gamma}_{i,w}^2} \leq \mu_i \hat{\gamma}_{i,n}}{\operatorname{argmin}} \; \mathbf{v}_{i,N}^T\left(\hat{\gamma}_{i,u}\mathbf{u}_i + \hat{\gamma}_{i,w}\mathbf{w}_i\right)
\end{aligned}
$$

$$(4.20)$$

In the system 4.19, $\mathbf{D}_i$ represents a tangent space generators $\mathbf{D}_i = \left[\mathbf{D}_{i,n}, \mathbf{D}_{i,u}, \mathbf{D}_{i,w}\right]$ defined as in equation 4.21, where $\mathbf{A}_{i,p}$ is the $\mathbb{R}^3$ matrix of local coordinates of the i^{th} contact, and $\tilde{\bar{s}}_{i,A}$ $\tilde{\bar{s}}_{i,B}$ represents the contact point positions in body relative coordinates.

$$
\mathbf{D}_i^T = \left[\mathbf{0} \ldots - \mathbf{A}_{i,p}^T \mathbf{A}_{i,p}^T \mathbf{A}_A \tilde{\bar{s}}_{i,A} \mathbf{0} \ldots \mathbf{0} \mathbf{A}_{i,p}^T - \mathbf{A}_{i,p}^T \mathbf{A}_B \tilde{\bar{s}}_{i,B} \ldots \mathbf{0}\right] \qquad (4.21)
$$

4.1.4 Time-stepping scheme

To integrate numerically this problem, the time-stepping formulation must be considered.

Given the generalize position $\mathbf{q}^{(l)}$ and velocity $\mathbf{v}^{(l)}$ at the time step $t^{(l)}$, the numerical solution at the new time-step $t^{(l+1)} = t^{(l)} + h$ can be found solving equation 4.22.

$$
\begin{aligned}
\mathbf{M}\left(\mathbf{v}^{(l+1)} - \mathbf{v}^{(l)}\right) &= h\mathbf{f}\left(t^{(l)}, \mathbf{q}^{(l)}, \mathbf{v}^{(l)}\right) + \\
&\quad \sum_{i \in \mathcal{A}\left(\mathbf{q}^{(l)}, \delta\right)} \left(\gamma_{i,n}\mathbf{D}_{i,n} + \gamma_{i,u}\mathbf{D}_{i,u} + \gamma_{i,w}\mathbf{D}_{i,w}\right) + \sum_{i \in \mathcal{B}} \gamma_{i,b} \nabla \mathbf{\Psi}_i \\
& i \in \mathcal{B} : \frac{1}{h}\mathbf{\Psi}\left(\mathbf{q}^{(l)}, t\right) + \nabla \mathbf{\Psi}_i^T \mathbf{v}^{(l+1)} + \frac{\partial \mathbf{\Psi}_i}{\partial t} = 0, \qquad (4.22) \\
& i \in \mathcal{A}\left(\mathbf{q}^{(l)}, \delta\right) : 0 \leq \frac{1}{h}\mathbf{\Phi}_i\left(\mathbf{q}^{(l)}\right) + \mathbf{D}_{i,n}\mathbf{v}^{(l+1)} \perp \gamma_n^i \geq 0 \\
\left(\gamma_{i,u}, \gamma_{i,w}\right) &= \underset{\sqrt{\hat{\gamma}_{i,u}^2 + \hat{\gamma}_{i,w}^2} \leq \mu_i \hat{\gamma}_{i,n}}{\operatorname{argmin}} \; \mathbf{v}^T\left(\gamma_{i,u}\mathbf{u}_i + \gamma_{i,w}\mathbf{w}_i\right)
\end{aligned}
$$

$$\mathbf{q}^{(l+1)} = \mathbf{q}^{(l)} + h\mathbf{L}\left(\mathbf{q}^{(l)}\right)\mathbf{v}^{(l+1)}$$

The problem above defined is a non-linear complementarity problem, where $\gamma_s = h\hat{\gamma}_s$ is the constraint impulse and $\frac{1}{h}\mathbf{\Phi}_i\left(\mathbf{q}^{(l)}\right)$ represents a constraint stabilization.

Introducing a relaxation over the complementarity constrain as shown in equation 4.23, the problem can be denoted as a cone complementarity problem (CCP), which can be efficiently solved by a family of iterative numerical methods, as shown by Anitescu and Tasora in [2].

$$\begin{aligned} & i \in \mathcal{A}\left(\mathbf{q}^{(l)}, \delta\right) \\ & 0 \leq \frac{1}{h}\mathbf{\Phi}_i\left(\mathbf{q}^{(l)}\right) + \mathbf{D}_{i,n}^T\mathbf{v}^{(l+1)} - \mu_i\sqrt{\left(\mathbf{v}^T\mathbf{D}_{i,u}^2 + \mathbf{v}^T\mathbf{D}_{i,w}^2\right)} \perp \gamma_n^i \geq 0 \end{aligned} \tag{4.23}$$

4.2 Simulations

The first issue to face is to correctly represent the soil behaviour. Thus a direct shear test has been simulated to set the soil parameters.

This test consists in measuring the shear resistance of a soil sample, as discussed in more detail in chapter 2 at section 2.1.2.

The soil is placed in a box divided at middle height in two part, sliding one respect the other at constant speed. The shear resistance of the soil is inferred from the force opposed to the displacement.

This test is repeated for different values of the normal pressure imposed to the soil sample, and the relationship between the pressure σ and the soil shear resistance τ_{max} is determined.

When the simulations presented in this section were carried out, the experimental tests, whose results are discussed in section 2.1.2, were not avalaible, thus the simulations refer to experimental data available in literature [30].

4.2.1 Simulation data

The experimental data, drawn from literature [30], are shown in figures 4.1 and 4.2.

In figure 4.1 is depicted the soil sample granulometry, which has been measured by three different methods as explained in [30]. The tested soil sample had been sieved with a No 10 sieve, hence the granulometry of pebbles for the simulations has been stated according with the corresponding curve of figure 4.1.

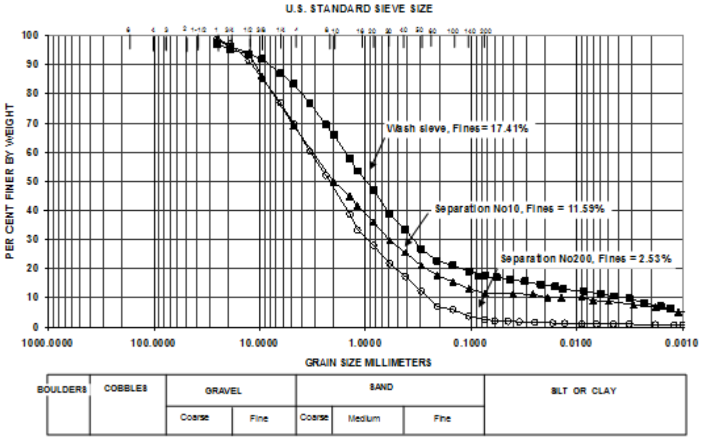

Figure 4.1: *soil sample granulometry [30].*

In the simulations data three different classes of pebbles had been defined according to figure 4.1, as shown in table 4.1. The density is the same for all the three classes and corresponds to the mean density of the sample, while the diameter sizes are selected to limit the total number of pebbles, thus the computational effort.

Table 4.1: *soil granulometry*

Number [-]	Mass Percentage [%]	Density [kg/m^3]	Diameter [m]
78	70	1700	0.020
630	15	1700	0.010
5042	15	1700	0.005

In figure 4.2 are draft the results of a series of direct shear tests, carried out for different pressure values, in order to state the relationship between the soil shear resistance, i.e. the maximun shear stress susteinable by the soil τ_{max}, and the pressure σ.

The simulations that are presented in this section are intended to reproduce the point at σ 100 kPa of the figure 4.2.

The pressure σ is imposed by putting over the pebbles a cover of 100 kg of mass, that put over a section of 0.1×0.1 m correspond to about 100 kPa of pressure.

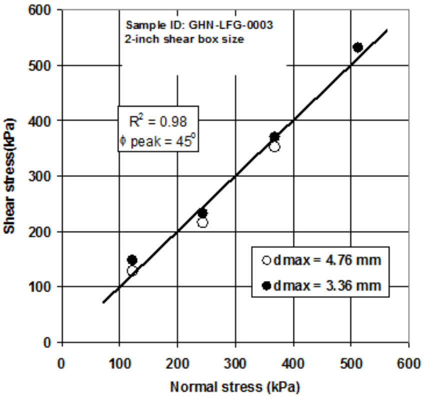

Figure 4.2: *shear resistance vs normal pressure [30].*

4.2.2 Simulation results

Three different simulations and their results will be discussed, in order to show the influence of simulation parameters on simulation results.

The simulation parameters are shown in table 4.2:

- The time step and the iterations number affect the simulation convergence: increasing the iterations number and decreasing the time step allow to improve the convergence, however it rises the computational effort, extending the execution time of the simulation.
- The recovery speed is the limit speed for two bodies that compenetrate to move away from each other.
- The warm start is a flag, that when activated imposes that the iteration at the next time step will start from the end of the previous step.
- Finally the friction coefficient is the coefficient $\mu_i \in \mathbb{R}^+$ of Coulomb theory.

Table 4.2: *simulations parameters*

		Simulation A	Simulation B	Simulation C
time step	[s]	0.0001	0.0005	0.0005
recovery speed	[m/s]	0.2	0.1	0.1
iterations number	[]	250	80	400
warm start	[]	false	true	false
friction coefficient	[]	0.7	0.8	0.8

The shear speed of the test has been set to 0.01 m/s; this value had been chosen to mediate between the need of limit the execution time and to choose a low speed, as prescripted by the norm [6].

Simulation A

The first simulation has been carried out for a mean iterations number and a small time step.

The simulation results will show that the simulation converged, although the shear resistance was lower than expected.

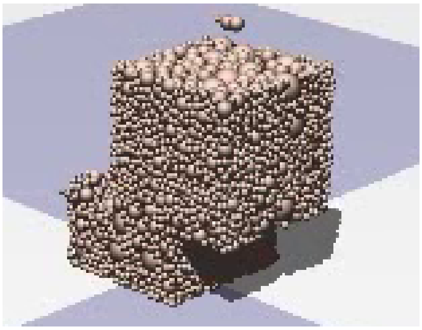

Figure 4.3: *pebbles in the shear box during the simulation A.*

Figure 4.3 shows the pebbles in the shear box after 5 s of simulations. It is possible to observe the presence of pebbles of three different dimensions and that among them three are locked over the cover, which is not depicted, and do not partecipate actively to the test.

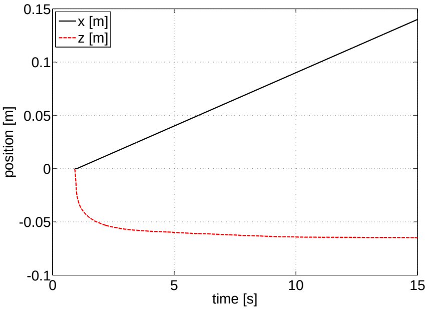

Figure 4.4: *cover vertical z and horizontal x position as a function of the simulation time, simulation A*

Figure 4.4 shows the cover vertical and longitudinal position during the test. It is possible to notice that the cover is not created at the beginning of the simulation, but after 0.9 s, to allow to the pebbles bulk to stabilize.

After that the cover is created and released over the pebbles, the vertical position z decreases rapidly, while the cover compress the pebbles sample, until the shear test begins after 1.0 s of simulation, when the upper box starts to slide, followed by the cover, as it is possible to notice from longitudinal position x.

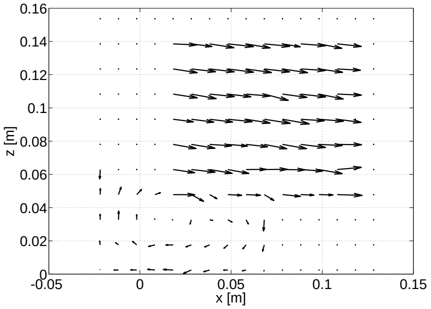

Figure 4.5: *pebbles speed vectors in the middle section of the soil sample, simulation A.*

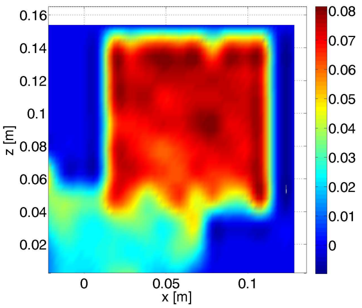

Figure 4.6: *pebbles speed modulus in the middle section of the soil sample, simulation A.*

As previously observed, that problem formulation allows to study the behaviour of the pebbles in the soil bulk; for istance in figures 4.5 and 4.6 the pebbles speed in the central section of the sample after 5s of simulation is shown.

Figure 4.5 shows the speed direction, while figure 4.6 shows the speed modulus. It is possible to notice that the pebbles in the upper part of the box are moving longitunally with the box, whereas the pebbles in the lower part of the shear box are spinning around the center of the soil bulk.

Figures 4.7 and 4.8 refer to the forces developed by the soil pebbles. The peaks are related to locking effects in the pebbles bulk, which happens when a pebble gets stuck among a wall and the other pebbles.

Figure 4.8 shown the load measured at the box floor. The total mass of the pebbles is 1.6772 kg, thus the initial value of the load is around 16.45 N and it is not noticeable in the draft scale. After 0.7 s the cover impacts on the pebbles bulk and at load measured at the box floor increases until 981 N, after that value the measured load decreases, because with the sliding movement of the upper part of the box, the cover load begins to drain on the lateral wall of the box instead that on the box floor. Finally after 11.0 s the lower and the upper part of the box are no longer in contact.

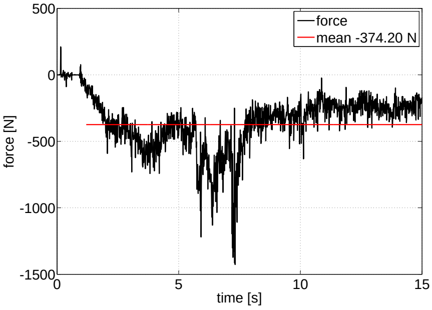

Figure 4.7: *shear resistance of the soil, simulation A.*

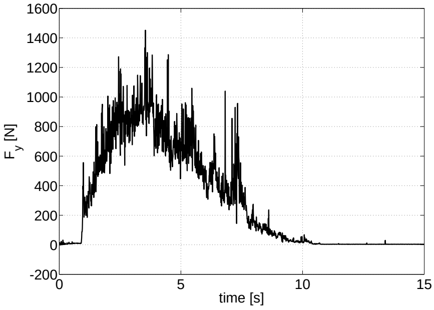

Figure 4.8: *load on the box floor, simulationi A.*

Figure 4.7 shows the force opposed by the soil pebbles to the sliding displacement of the upper part of the box. The shear resistance is negative because it is opposed to the motion direction, which is accounted to be positive. The maximum value of that force is around 800 N, corresponding to 80 kPa of a shear section of 0.1×0.1 m, which is lower that the expeted result of 100 kPa.

Hence the next simulation had been set considering a higher value of the friction parameter.

Simulation B

To decrease the computational effort of the simulation, simulation B has been carried out decreasing the number of iteration and increasing the time step. The warm start has been set on, in order to study its influence on the simulation convergence. The simulation time has been reduced, since from simulation A it has been possible to notice that the maximum shear force is reached at about 7.0 s.

Figures 4.9 and 4.10 show the pebbles speed in the middle section of the pebbles bulk. The figures refer to the beginning of the simulation, when the cover impacts on the pebbles, compressing them. Thus the pebbles are moving toward the bottom of the box: the speed decreases from the top to the bottom, where the pebbles are stopped by the box floor.

Figures 4.11 and 4.12 refer respectively to the shear resistance and to the load measured at box floor.

Similarly to figure 4.8, figure 4.12 shows the load measured at the box floor; it is possible to notice two main peaks at the begininning and at the end of the simulation. The first peak is due to the impact of the cover on

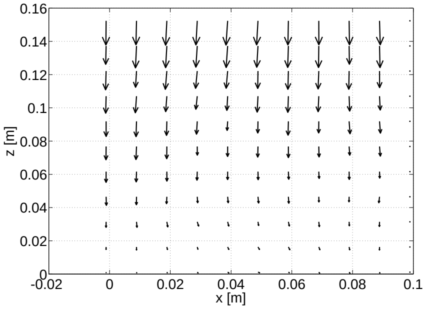

Figure 4.9: *pebbles speed vectors in the middle section of the soil sample, simulation B.*

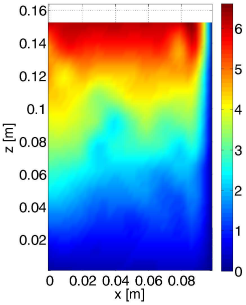

Figure 4.10: *pebbles speed modulus in the middle section of the soil sample, simulation B.*

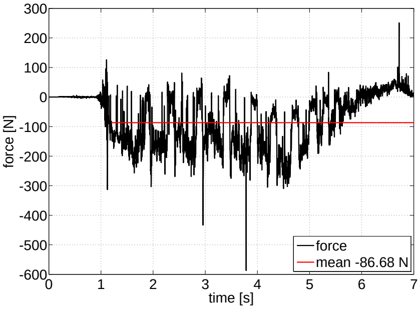

Figure 4.11: *shear resistance of the soil, simulation B.*

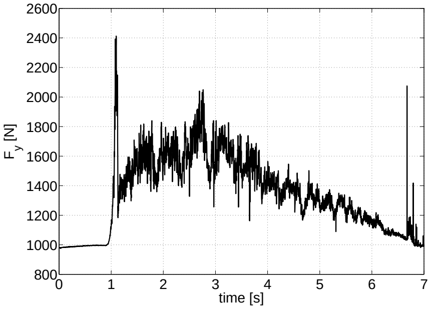

Figure 4.12: *load on the box floor, simulationi B.*

the pebbles bulk, whereas the last one is likely to be caused by the locking effect of a pebble stucks between the upper and the lower parts of the box, indeed it is possible to see a peak a the same time also in figure 4.11.

Figure 4.11 shows the shear resistance of the soil. Besides the reduction of mean value, it is possible to observe a marked discontinuity in the force.

Since the warm start has been actived, if two pebbles enter in contact at time step t_i, at the next time steps the speed computed starting from the results of the previous step is not zeroed, and the pebbles keep to approach each other, until the compenetration imposes to the pebbles is enough big to make the pebbles run away from each other at recovery speed. When the pebbles are strayed the gravity or the impact with other pebbles make them coming back, and the phenomenon repeats.

Because of the instability it introduces in the convergence, the warm start had been turn off in the next simulation.

Simulation C

Simulation C had been carried out increasing the number of iterations and turning off the warm start. However the results present a problem of convergence, indeed the recovery speed is too low in these conditions and the pebbles compenetrate, as it is possible to observe in figure 4.13.

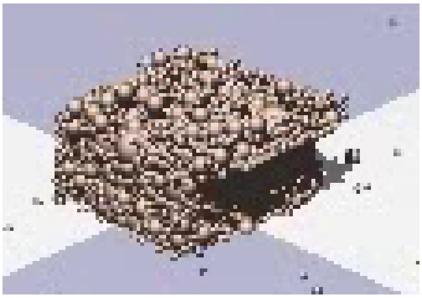

Figure 4.13: *pebbles in the shear box during the simulation C.*

Figure 4.14 shows the cover position during the simulation. As in figure 4.4 it is possible to observe that the cover is not created at the beginning of the simulation, but after 0.9 s, to allow to the pebbles bulk to stabilize.

Figures 4.15 and 4.16 shows the pebbles speed in the middle section of the bulk after 0.95 s, when the cover already compresses the pebbles, but the shear movement of the upper part of the box is not begun.

It is possible to observe that the speed is higher at the top of the bulk. This effect is due to the impact of the cover, that compenetrate the pebbles, which start to move away at recovery speed. Hovever the pebbles start

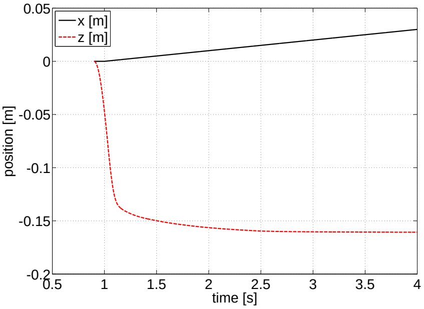

Figure 4.14: *cover vertical z and horizontal x position as a function of the simulation time, simulation A*

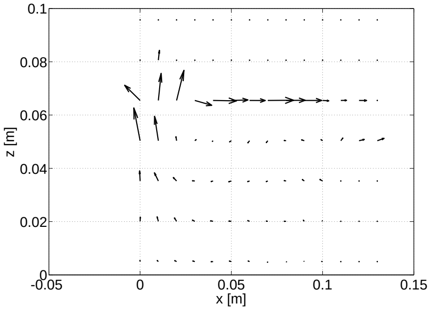

Figure 4.15: *pebbles speed vectors in the middle section of the soil sample, simulation C.*

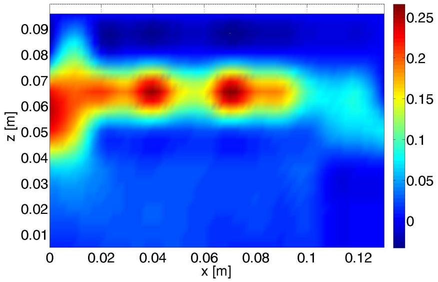

Figure 4.16: *pebbles speed modulus in the middle section of the soil sample, simulation C.*

to move away after an excessive level of compenetration, how it can be noticed from figure 4.13, where is is possible to observe that the pebbles are compenetrating and the total volume of the bulk is innaturally reduced.

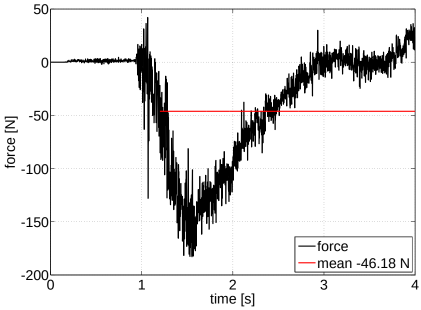

Figure 4.17: *shear resistance of the soil, simulation C.*

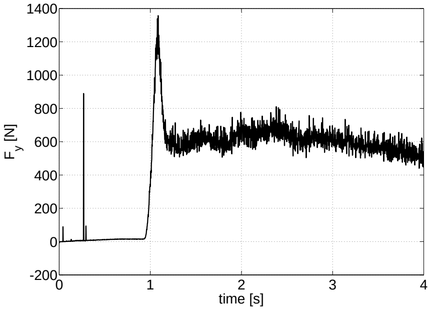

Figure 4.18: *load on the box floor, simulationi C.*

As a consequence of these issues, the shear resistance of the soil is low than the expected value of about 100 kPa, as it can be noticed from the force opposed to the shear displacement drawed in figure 4.17, whereas the load at the box floor is correctly measured, as it is possible to infer from figure 4.18.

4.2.3 Conclusions

The simulation results shown in the previous section (sec. 4.2.2) allow to point out the possibilities offered by this model; indeed it allows to visualize the displacements and reaction forces in the middle of the soil bulk, thus the analysis if not limited to the topsoil surface.

To improve this model, a new iterative method should be accounted to integrate the solution, since the mass differece between the pebbles and the upper load stiffen the problem rising the computation effort.

Moreover to investigate the influence of the pebbles size over the shear resistance, the number of particles should be increased and thus their dimensions reduced, leading to a higher computational effort.

A further advantage of the dvi formulation provided by the Chrono::Engine library is that it can be applied to a large amount of problem.

For instance, this Chrono::Engine library has been used to simulate the separation of electronic waste by an eddy current separator [16]. This machinery is composed by a conveyor belt, at the end of which is placed a rotor with a number of alternating N/S magnetic poles. The waste is distributed on the conveyor belt and when the metallic particles approach the magnetic field, eddy currents are induced, thus the metallic particles are accelerated whereas the nonconductive particles are not affected by the magnetic field and fall close to the drum under the gravitational force. The dvi formulation allows to simply consider the effect of the impact on the particles fall and separation.

The developement of a model base on the Chrono::Engine library can lead to an improvement in subsoil simulation, although a more efficient solver is required to simulate a large amount of pebbles organized in superposed layers under an elevate load, despite the use of GPU units for the calculation.

CHAPTER 5

Conclusions

The aim of this thesis were to supply a tool able to model the interaction between tyre and soil, considering tyre geometrical and structural properties and soil characteristics.

In particular experimental tests has been carried out to infer soil and tyre characteristics.

The tyre structure has been modeled by means of a modal model, whose parameters have been identify through an impulsive test, allowing to infer the eigenvalues and eigenfrequencies of the tyre.

The soil has been characterized in shear and normal responses by two tests: the direct shear test, performed to measure the shear resistance of a soil under pressure, and the cone penetrometer test, allowing to measure the normal resistance of the soil to the sinkage of a conic pin.

Through those tests it has been possible to set the parameters of a numerical model of the tyre-soil interaction, based on matlab language.

The forces exchanged between tyre an soil had been calculated considering the sinkage and the shear displacement due to the tyre forward displacement.

This plane model allowed to simulate the ride of a tyre over a loose soil, with a satisfying level of confidence. Furthermore it has been used to carry out a sensitivity analysis of a tread greometry, showing the influence of lugs shape and dimension on tractive performance, comfort, and soil sinkage.

Moreover, a multi-body particles model has been stated to represent the soil dynamics. This model is based on a multi-body C++ library, called Chrono::Engine, using the differential variational inequalities theory to integrate the particles interaction forces and displacements.

This model allows to consider the soil displacement and stress distribution in subsoil layers, and the tridimensionality of the problem.

This particles model can allow to point out how the topsoil strain and stress affect the subsoil layers.

In this thesis this model has been used to simulate the direct shear test carried out on a soil sample, in order to correctly set the parameters to simulate the soil dynamics.

List of Figures

1.1 stress distribution beneath a tyre at rest [40] 3
1.2 the distribution of the amount of slippage under a rigid wheel at driving state [40] 5
1.3 the trajectory of a point F on the peripherical surface of the wheel at driving state [40] 5
1.4 the distribution of the amount of slippage under a rigid wheel at braking state [40] 7
1.5 the trajectory of a point F on the peripherical surface of the wheel at braking state [40] 8
1.6 three different models of the contact surface shape between tyre and soil [49] 10
1.7 the four tread pattern tested by Rodriguez and alt [47] 15

2.1 Conic penetrometer. 18
2.2 test results: resistence of the soil as a function of the penetrometer sinkage. 19
2.3 direct shear box apparatus [40]. 20
2.4 relationship between shear stress and shear displacement. . . 21
2.5 relationship between shear stress and normal stress. 21
2.6 direct shear test results. 22
2.7 Placement of the accelerometer sensors during the impulsive test of the tyre. 23
2.8 expected modes shapes for cross-ply tyre [29] 23
2.9 filtering function of the hammer used to excite the tyre. . . . 24

2.10 shape of the modal deformates indentified 28
2.11 Traction force available as a function of the slip on the tractive tyres 29

3.1 the different orientation of the four surfaces modelling the tread pattern along a section of the tyre, and the references of normal and shear stresses. 33
3.2 the tread pattern has been divided by a grid, and each element of the grid has been associated with the areas covered by the four surfaces as shown for the element pointed out by way of example. 33
3.3 The image of the tread pattern after preprocessing 34
3.4 scheme of the tyre structure model 38
3.5 normal stress as a function of the sinkage: assuming that a soil has been compressed at $z^{'}$, the unload phase from $z^{'}$ to $z^{''}$ and further load phases back to $z^{'}$ are described through a different linear relation whose slope K_{II} is higher than K_I 40
3.6 the slip velocity reference and component depending on the surface orientation. 42
3.7 the shear stress is a function of the shear stress and of the pressure: the experimental results have been interpooled with analytical expression. 43
3.8 the shear stress is a function of the shear stress and of the pressure: increasing pressure and displcement, the shear stress increases. 43
3.9 position of the center of the k^{th} area of the i^{th} element of the grid 44
3.10 traction force available as a function of slip and of inflation pressure 46
3.11 soil sinkage as a function of slip and of inflation pressure. . . 47
3.12 standard deviation of the hub vertical acceleration as a function of slip and of inflation pressure. 47
3.13 tread pattern modulus 48
3.14 traction force as a function of lugs number and angle, for center length of 64 mm and 5% of slip 49
3.15 traction force as a function of lugs number and angle, for center length of 64 mm and 25% of slip 49
3.16 traction force as a function of lugs number and angle, for center length of 72 mm and 5% of slip 49

3.17 traction force as a function of lugs number and angle, for center length of 72 mm and 25% of slip 49
3.18 traction force as a function of lugs number and angle, for center length of 80 mm and 5% of slip 50
3.19 traction force as a function of lugs number and angle, for center length of 80 mm and 25% of slip 50
3.20 traction force as a function of lugs number and angle, for center length of 88 mm and 5% of slip 50
3.21 traction force as a function of lugs number and angle, for center length of 88 mm and 25% of slip 50
3.22 traction force as a function of lugs number and angle, for center length of 96 mm and 5% of slip 50
3.23 traction force as a function of lugs number and angle, for center length of 96 mm and 25% of slip 50
3.24 standard deviation of the hub vertical acceleration σ_z as a function of lugs number and angle, for center length of 64 mm and 5% of slip 52
3.25 standard deviation of the hub vertical acceleration σ_z as a function of lugs number and angle, for center length of 64 mm and 25% of slip 52
3.26 standard deviation of the hub vertical acceleration σ_z as a function of lugs number and angle, for center length of 72 mm and 5% of slip 52
3.27 standard deviation of the hub vertical acceleration σ_z as a function of lugs number and angle, for center length of 72 mm and 25% of slip 52
3.28 standard deviation of the hub vertical acceleration σ_z as a function of lugs number and angle, for center length of 80 mm and 5% of slip 53
3.29 standard deviation of the hub vertical acceleration σ_z as a function of lugs number and angle, for center length of 80 mm and 25% of slip 53
3.30 standard deviation of the hub vertical acceleration σ_z as a function of lugs number and angle, for center length of 88 mm and 5% of slip 53
3.31 standard deviation of the hub vertical acceleration σ_z as a function of lugs number and angle, for center length of 88 mm and 25% of slip 53

3.32 standard deviation of the hub vertical acceleration σ_z as a function of lugs number and angle, for center length of 96 mm and 5% of slip 54
3.33 standard deviation of the hub vertical acceleration σ_z as a function of lugs number and angle, for center length of 96 mm and 25% of slip 54
3.34 maximum sinkage as a function of lugs number and angle, for center length of 64 mm and 5% of slip 55
3.35 maximum sinkage as a function of lugs number and angle, for center length of 64 mm and 25% of slip 55
3.36 maximum sinkage as a function of lugs number and angle, for center length of 72 mm and 5% of slip 55
3.37 maximum sinkage as a function of lugs number and angle, for center length of 72 mm and 25% of slip 55
3.38 maximum sinkage as a function of lugs number and angle, for center length of 80 mm and 5% of slip 56
3.39 maximum sinkage as a function of lugs number and angle, for center length of 80 mm and 25% of slip 56
3.40 maximum sinkage as a function of lugs number and angle, for center length of 88 mm and 5% of slip 56
3.41 maximum sinkage as a function of lugs number and angle, for center length of 88 mm and 25% of slip 56
3.42 maximum sinkage as a function of lugs number and angle, for center length of 96 mm and 5% of slip 57
3.43 maximum sinkage as a function of lugs number and angle, for center length of 96 mm and 25% of slip 57
3.44 tested vehicle on the four-post test rig. 59
3.45 multi-body vehicle model 59
3.46 cabin heave accelerations during a sweep sine test with all the actuators moved in phase. Front suspension switched off. 60
3.47 cabin heave accelerations during a sweep sine test with all the actuators moved in phase. Front suspension switched on. 60
3.48 cabin pitch accelerations during a sweep sine test with front and rear actuators moved in counter phase. Front suspension switched off. 61
3.49 cabin pitch accelerations during a sweep sine test with front and rear actuators moved in counter phase. Front suspension switched on. 61

3.50 tread pattern of the tyre modeled for the simulations performed considering the interaction with a multi-body model of the whole tractor 62
3.51 soil deformation after the tractor passage 63
3.52 interaction forces between the soil and the tyre 63
3.53 standard deviation of the vertical acceleration of the driver seat as a function of cabin and seat damping 64

4.1 soil sample granulometry [30]. 72
4.2 shear resistance vs normal pressure [30]. 73
4.3 pebbles in the shear box during the simulation A. 74
4.4 cover vertical z and horizontal x position as a function of the simulation time, simulation A 74
4.5 pebbles speed vectors in the middle section of the soil sample, simulation A. 75
4.6 pebbles speed modulus in the middle section of the soil sample, simulation A. 75
4.7 shear resistance of the soil, simulation A. 76
4.8 load on the box floor, simulationi A. 76
4.9 pebbles speed vectors in the middle section of the soil sample, simulation B. 77
4.10 pebbles speed modulus in the middle section of the soil sample, simulation B. 77
4.11 shear resistance of the soil, simulation B. 77
4.12 load on the box floor, simulationi B. 77
4.13 pebbles in the shear box during the simulation C. 78
4.14 cover vertical z and horizontal x position as a function of the simulation time, simulation A 79
4.15 pebbles speed vectors in the middle section of the soil sample, simulation C. 79
4.16 pebbles speed modulus in the middle section of the soil sample, simulation C. 79
4.17 shear resistance of the soil, simulation C. 80
4.18 load on the box floor, simulationi C. 80

List of Tables

2.1 cone index required for construction machine trafficability [40] 19
2.2 parameters of the tyre structure 28

3.1 parameters of the equation 3.32 interpolating the direct shear test results 43
3.2 comparison between numerical and experimental results of a traction test 47
3.3 variation of the tread pattern parameters 48
3.4 stiffness and damping of the tractor model 59
3.5 stiffness and damping of the tyres 62
3.6 North Gower sandy loam soil properties 62

4.1 soil granulometry 72
4.2 simulations parameters 73

Bibliography

[1] M. Anitescu and F. A. Potra. Formulating dynamic multi-rigid-body contact problems with friction as solvable linear complementarity problems. Nonlinear Dynamics, 14:2331–247, 1997.

[2] M. Anitescu and A. Tasora. An iterative approach for cone complementarity problems for nonsmooth dynamics. Computational Optimization and Applications, 47(2):207–235, 2010.

[3] J. Arvidsson and T. Keller. Soil stress as affect by wheel load and tyre inflation pressure. Soil Till Res, 96(1-2):284–291, 2007.

[4] J. Arvidsson and S. Ristic. Soil stress and compaction effect for four tractor tires. J Terramechanics, 33(5):223–232, 1996.

[5] J. Arvidsson, H. Westlin, T. Keller, and M. Gilbertsson. Rubber track systems for conventional tractor - effects on soil compaction and traction. Soil Till Res, 117:103–109, 2011.

[6] ASTM International, West Conshohocken, PA. Standard Test Method for Direct Shear Test of Soils Under Consolidated Drained Conditions, astm standard d3080/d3080m edition, 2011.

[7] T. Aubel. Application of finite-element methos on soil mechanical processes. In 5th European Conference of the ISTVS, 1991.

[8] T. Aubel. Fem simulation of the interaction between an elastic tyre and soft soil. In 11th Intenational Conference of the ISTVS, 1993.

[9] T. Aubel. The interaction between the rolling tyres and the soft soil fem simulation by venus and validation. In 6th European Conference of the ISTVS, 1994.

[10] M.G. Bekker. Theory of land locomotion - The mechanics of vehicle mobility. The University of Michigan Press, Ann Arbor, 1962.

[11] G.F. Botta, D. Jorajuria, R. Balbuena, and H. Rosatto. Mechanical and cropping behaviour of direct drilled soil under different traffic intensities: effect on soybean (glycine max l.) yields. Soil Till. Res., 78(1):53–58, 2004.

[12] G.F. Botta, D. Rivero, M. Tourn, F. Bellora Melcon, O. Pozzolo, G. Nardon, R. Balbuena, A. Tolon Becerra, H. Rosatto, and S. Stadler. Soil compaction produced by tractor with radial and cross-ply tyres in two tillage regimes. Soil Till Res, 101(1-2):44–51, 2008.

[13] G.F. Botta, A. Tolon-Becerra, M. Tourn, X. Lastra-Bravo, and D. Rivero. Agricultural traffic: motion resistance and soil compaction in relation to tractor design and different soil condition. Soil Till Res, 120:92–98, 2011.

[14] F. Braghin, F. Cheli, M. Colombo, E. Sabbioni, C. Bisaglia, and M. Cutini. Characterization of the vertical dynamic behaviour of an agricultural vehicle. In Proceedings the ECCOMAS Thematic Conference in Multibody Dynamics, Milan, Italy, June 2007.

[15] F. Braghin, F. Cheli, S. Melzi, S. Negrini, and E. Sabbioni. A 3d multibody model of an agricultural vehicle operating on a deformable soil: numerical investigation of the vertical dynamics. In Proceedings the ECCOMAS thematic conference in multibody dynamics, Bruxelles, Belgium, July 2011.

[16] F. Braghin, M. Colledani, S. Negrini, and A. Tasora. A multi-body, multi-particle simulation model of eddy current separation (ecs) process for recycling. In Proceedings the SUM 2012 - Symposium on Urban Mining, Bergamo, Italy, May 2011.

[17] F. Braghin, A. Genoese, E. Sabbioni, C. Bisaglia, and M. Cutini. Experimental evaluation of different suspension systems for agricultural vehicles through four-poster test bench. In Proceedings of 11th VSDIA Conference, Budapest, Hungary, 2008.

[18] F. Braghin, S. Melzi, and S. Negrini. Soil model for agricultural tire ground interaction simulation. In 12th Mini Conference on Vehicle System Dynamics Identification and Anomalies (VSDIA 2010), Budapest, Hungary, November 2010.

[19] F. Braghin, S. Melzi, S. Negrini, and E. Sabbioni. Prediction of the maximum traction force for agricultural tyres as a function of tread number. In 12th Mini Conference on Vehicle System Dynamics Identification and Anomalies (VSDIA 2010), Budapest, Hungary, November 2010.

[20] M.V. Braunack. A tyre option for sugarcane haulout trucks to minimize soil compaction. J Terramechanics, 41(4):243–253, 2004.

[21] L. Clijmans, H. Ramon, J. Langenakens, and J. De Baerdemaeker. The influence of tyres on the dynamic behavior of a lawn mower. J Terramechanics, 33(4):195–208, 1996.

[22] P.A. Cundall. Computer model for simulating progressive large scale movements in blocky systems. In Proceeding of the Symposium of the international society for Rock mechanics, 1971.

[23] E. Diserens. Calculating the contact area of trailer tyres in the field. Soil till Res, 103(2):302–209, 2009.

[24] D.J. Edwins. Modal Testing: Theory, Practice and Application. John Wiley & Sons, New York, 1999.

[25] K.A.A. El-Gawwad, D.A. Crolla, A.M.A. Soliman, and F.M. El-Sayed. Off-road tyre modelling i: the multi-spoke tyre model modeified to include the effect of straight lugs. J Terramechanics, 36(1):3–24, 1999.

[26] K.A.A. El-Gawwad, D.A. Crolla, A.M.A. Soliman, and F.M. El-Sayed. Off-road tyre modelling ii: effect of camber on tyre performance. J Terramechanics, 36(1):25–38, 1999.

[27] K.A.A. El-Gawwad, D.A. Crolla, A.M.A. Soliman, and F.M. El-Sayed. Off-road tyre modelling iii: effect of angled lugs on tyre performance. J Terramechanics, 36(2):63–75, 1999.

[28] A. Gibbesch and R. Krenn. Planetary rover mobility performance simulation on a sandy terrain. Simpack news, pages 8–11, November 2009.

[29] D.H. Guan, L.H. Yam, M.P. Mignolet, and Y.Y. Liy. Experimental modal analysis of tyres. Experimental techniques, 24:39–45, 2000.

[30] L.A. Fernandes Gutierrez. The influence of mineralogy, chemistry and physical engineering properties on shear strength parameters of the goathill rock pile material, questa molybdenum mine, new mexico. Master's thesis, New Mexico Institute of Mining and Technology, 2006.

[31] A. Jain, J. Balaram, J. Cameron, J. Guineau, C. Lim, M. Pomerantz, and G. Sohl. Recent developmentes in the roams planetary rover simulation environment. In IEEE 2004 Aerospace Conference, Big Sky, Montana, March 2004.

[32] Z. Janamoto and B. Hanamoto. An analysis of the drawbar pull vs slip relationship for track laying vehicles. Technical report, U.S. Army Ordnance Tank-Automotive Command, 1961.

[33] F. Jin, C. Zang, W. Hu, and J. Wang. 3d mode discrete element method: elastic model. Int J of Rock Mech Min, 48:59–66, 2011.

[34] M.I. Lyasko. How to calculate the effect of soil condition on tractive performance. J Terramechanics, 47(6):423–445, 2010.

[35] J. Matthews. Ride comfort for tractor operators. J. agric. Eng. Res., 11(1):44–57, 1966.

[36] H. Mazhar. Parallel multi-body dynamics on graphics processing unit (GPU) cards. PhD thesis, University of Wisconsin-Madison, 2012.

[37] E. McKeys. Soil cutting and tillage. Elsevier Science, 1985.

[38] S. Milosavljevic, D.I. McBride, N. Bagheri, R.M. Vasiljev, R. Mani, A.B. Carman, and B. Rehn. Exposure to whole-body vibration and mechanical shock: a field study of quad bike use in agriculture. Ann. Occup. Hyg., 55(3):286–295, 2011.

[39] A. Mohsenimanesh, S.M. Ward, P.O.M. Owende, and A. Javadi. Modelling of pneumatic tractor tyre interaction with multi-layered soil. Biosystem Engineering, 104(2):191–198, 2009.

[40] T. Muro and J. O'Brien. Terramechanics: land locomotion mechanics. Taylor & Francis Group, 2004.

[41] V.N. Nguyen and S. Inaba. Effects of tire inflation pressure and tractor velocity on dynamic wheel load and rear axle vibrations. J Terramechanics, 48(1):3–16, 2011.

[42] V.N. Nguyen, T. Matsuo, S. Inaba, and T. Kuomoto. Experimental analysis of vertical soil reaction and soil stress distribution under off-road tires. J Terramechanics, 45(1-2):25–44, 2008.

[43] R. Olson, D.I. Hahn, and A. Buckert. Predictors of severe trunk postures among short-haul truck drivers during non-driving task: an exploratory investigation involving video assessment and driver behavioural self-monitoring. Ergonomics, 52(6):707–722, 2009.

[44] T.C. Palancar, A.M. Terminiello, and D. Jorajuria. Determinacion expeditiva del area del contecto rueda-suelo en maquinas agricolas. Universitad National de la Plata, 2001.

[45] J.S. Pang and D.E. Stewart. Differential variational inequalities. Mathematical programming, 113:1–80, 2008.

[46] D. Riverod, M. Tourna, F. Bellora Melcona, O. Pozzolo, G. Nardong, R. Balbuenae, A. Tolon Becerraf, H. Rosatto, and S. Stadlerd. Soil compaction produced by tractor with radial and cross-ply tyres in two tillage regimes. Soil Till Res, 101(1-2):44–51, 2008.

[47] L.A. Rodriguez, J.J. Valencia, and J.A. Urbano. Soil compaction and tires for harvesting and transporting sugarcane. J Terramechanics, 49(3-4):183–189, 2012.

[48] E. Sabbioni, S. Negrini, F. Braghin, and S. Melzi. A 2d model for tractor tire-soil interaction: Evaluation of the maximum traction force and comparison with experimental results. SAE Technical Paper, 1, 2011.

[49] I.C. Schmid. Interaction of vehicle and terrain results for 10 years research at ikk. J Terramechanics, 32(1):3–26, 1995.

[50] P. Servadio, A. Marsili, and N.P. Belfiore. Analysis of driving seat vibration in high forward speed tractors. Biosystem Engineering, 97(2):171–180, 2007.

[51] A.A. Shabana. Dynamics of multibody systems. Cambridge University Press, 2005.

[52] T. Smerda and J. Cupera. Effects of tire inflation pressure and tractor velocity on dynamic wheel load and rear axle vibrations. J Terramechanics, 47(1):395–400, 2010.

[53] G. Sohl and A. Jain. Wheel-terrain contact modeling in the roams planetary rover simulation. In IDETC'05, ASME International Design Technical Conference and Computers and Informations in Engineering Conference, Long Beach, California, September 2005.

[54] D.E. Stewart and J.C. Trinkle. An implicit time-stepping scheme for rigid-body dynamics with inelastic collisions and Coulomb friction. International Journal for Numerical Methods in Engineering, 39:2673–2691, 1996.

[55] T.R. Way, D.C. Erbach, A.C. Bailey, E.C. Burt, and C.E. Johnson. Soil displacement beneath an agricultural tractor drive tire. J Terramechanics, 42(1):35–46, 2005.

[56] T.R. Way, T. Kishimoto, K.A. Torbert, E.C. Burt, and A.C. Bailey. Tractor tire aspect ratio effects on soil bulk density and cone index. J Terramechanics, 46(1):27–34, 2009.

[57] K. Xia. Finite element modeling of tire/terrain interaction: application to predicting soil compaction and tire mobility. J Terramechanics, 48(2):113–123, 2011.